Wave impact pressure and kinematics due to breaking wave impingement on a monopile

Mayilvahanan Alagan Chella[1]*, Hans Bihs[2], Dag Myrhaug[3]
[1]Department of Civil and Environmental Engineering and Earth Sciences
University of Notre Dame, Notre Dame, Indiana 46556, USA
[2]Department of Civil and Environmental Engineering
[3]Department of Marine Technology
Norwegian University of Science and Technology (NTNU), 7491 Trondheim, Norway

Journal of Fluids and Structures, 2019, **86** , pp. 94-123.

Abstract

Breaking wave impact on a vertical cylinder in shallow waters is investigated numerically with the two-phase flow computational fluid dynamics model REEF3D. The model is based on the incompressible Reynolds-Averaged-Navier-Stokes (RANS) equations together with the level set method (LSM) and $k-\omega$ turbulence model. The spatial and time development of the maximum wave impact pressure and the associated velocity components are examined. Further, the breaking wave characteristics and geometric properties are evaluated with two-dimensional simulations. Comparisons of numerical results and experimental data indicate good agreement for free surface elevations and the characteristics at breaking and the breaking wave forces. A total of 9 two-dimensional and 27 three-dimensional simulations are performed to investigate the influence of the incident wave characteristics, wave impact conditions and breaker types on the maximum wave impact pressure and kinematics. The factors influencing the spatial and temporal variability of the vertical distribution for the maximum impact pressure and kinematics are investigated. Three impact conditions are considered in this study: (1) the wave with a vertical front breaks at the cylinder, (2) the broken wave hits the cylinder with a moderately developed overturning wave crest, and (3) the broken wave impacts the cylinder with a fully developed overturning wave crest. Further, the vertical and longitudinal variations of the maximum impact pressure during the breaking wave impact on the monopile are assessed. The numerically simulated free surface deformations during the wave impact are also presented and discussed. Finally, the total breaking wave force and the maximum impact pressure are analyzed for spilling and plunging b1reakers under different wave impact conditions.

Keywords:

Breaking waves, wave impact pressure, breaking kinematics, breaking characteristics, breaking wave forces, wave impact conditions, spilling and plunging breakers

*Corresponding author, malaganc@nd.edu
Postprint, published in Journal of Fluids and Structures, doi: http://dx.doi.org//10.1016/j.jfluidstructs.2019.01.016

1 Introduction

Offshore wind energy has become an attractive source of clean and renewable energy. As wind conditions in shallow waters offer potential sites for offshore wind turbines (OWT), most recent offshore wind farms are deployed close to the shoreline. Large monopile concepts are considered to be appropriate foundations for the next-generation OWT (6-8MW) in shallow and intermediate waters. Wave breaking in shallow waters is always combined with shoaling, as the wave motion is strongly influenced by the seabed. According to Camp et al. (2003), hydrodynamic loads from breaking waves have a large influence on global dynamic responses of OWT structures. Importantly, the associated hydrodynamics are rather complicated to understand compared to wave breaking in deep water (Lin, 2008). The total force and moment acting on a structure provides the design criteria for the global structural stability, whereas the local impact pressures of high magnitude with short duration govern both the design stresses of the local members in the impact region and the global stability of a structure. In particular, impulsive loads of short duration from wave breaking against substructures are generally much larger than the quasi-static forces and they may cause permanent structural deflections and damage to local structural elements (Alagan Chella et al., 2012). Together with the local impact loads, the breaking wave kinematics represent the flow scenario associated the wave impact problem. A complete cycle of the wave breaking process consists of several stages from the onset of breaking to fully broken waves in the surf zone. Extreme free surface topology changes take place during the breaking process such as the development of a nearly vertical wave front, the formation of the forward curling wave crest or water jet, the impingement of the water jet onto the free surface water, and the splash-up (Basco, 1985).

Laboratory experiments have contributed to a large extent to the present knowledge of breaking wave forces on slender cylinders (e.g. Goda et al. (1966); Sawaragi and Nochino (1984); Zhou et al. (1991); Chan et al. (1995); Wienke and Oumeraci (2005); Arntsen et al. (2011); Hildebrandt (2013)). However, measurements of velocity and acceleration under breaking waves and their interaction with structures in a controlled experiment are more demanding. Meanwhile, the theoretical estimation of the impact force mainly depends on the wave celerity and the curling factor at the wave impact which have to be determined from laboratory experiments. The computations of the breaking wave-structure interaction problem can be performed accurately using computational fluid dynamics (CFD) models without considering empirical breaking conditions, force coefficients and the assumptions regarding the shape of the wave profile at breaking. There have been several numerical studies in literature on modeling the interaction of breaking waves with vertical cylinders and the associated forces (see e.g. Christensen et al. (2005); Bredmose and Jacobsen (2010); Choi et al. (2015); Kamath et al. (2016); Ghadirian et al. (2016)). Christensen et al. (2005) attempted to model wave forces and wave run-up due to breaking waves in shallow waters with a Navier-Stokes (NS) solver and the Volume-of-Fluid (VOF) method. Bredmose and Jacobsen (2010, 2011) performed simulations with the open-source CFD model OpenFOAM based on the NS equations and the VOF method to study the wave impact on monopiles and inspection platforms of OWTs. Hildebrandt (2013) computed breaking wave impact pressures on a tripod structure subjected to breaking focused waves under three impact conditions using the commercial software ANSYS CFX, which is based on the VOF method. He found that the maximum impact pressure and shorter rise time occur for the impact condition when a steep wave front impinges the main leg of the tripod.

Ochi and Tsai (1984) analysed wave impact pressure from deep water wave breaking by considering two impact conditions, namely for wave breaking immediately ahead of a cylinder and for wave breaking far ahead of a cylinder. Later, Zhou et al. (1991) and Chan et al. (1995) experi-

mentally investigated wave impact pressures on a vertical cylinder for five different wave impact conditions. They found that the maximum pressure on the vertical cylinder was observed for the impact condition when the wave breaks before the cylinder and interacts with a moderately developed overturning wave crest. This was also later confirmed by Wienke and Oumeraci (2005) who performed large scale experiments to measure wave impact pressures and forces on a vertical cylinder from breaking focused wave packets. The free surface flow features that evolved during the breaking process were well represented in the numerical simulations using the open-source hydrodynamics model REEF3D (Bihs et al., 2016*a*), which is based on a CFD approach for spilling and plunging breakers over slopes as reported by Alagan Chella et al. (2016). Particularly, the wave characteristics and kinematics of a wave varying drastically during the breaking process play a vital role in determining the intensity of the impact. Kamath et al. (2016) modelled five different wave impact conditions and the resulting total breaking wave forces on a vertical cylinder using REEF3D. The computed results were in good agreement with the measured data reported by Irschik et al. (2002). Further, the study was extended by Bihs et al. (2016*b*) to examine the effect of wave impact conditions on breaking wave forces on a pair of vertical cylinders placed in tandem arrangement. The main findings of both studies were consistent with the results of the above mentioned experimental studies. They also reported that the breaking location with respect to the cylinder location is one of the most influential parameters that determines the wave impact force and its characteristics. However, these studies focused only on investigating total wave forces on structures.

Since the wave impact is a localized phenomenon, the wave impact pressure highly depends on the changes in the local kinematics during the impact (Chan et al., 1995). Hence, the fluid velocities associated with wave impact events need to be represented accurately for the evaluation of breaking wave loads. The impact load characteristics are very sensitive to the incident wave characteristics and the wave impact conditions. In fact, both parameters are related to the breaker height (H_b), the breaker type, the shape of the wave profile and fluid velocity at the impact. On the other hand, the vertical distribution of the wave impact pressure varies significantly for different breaker types. Although extensive experimental and numerical research have been performed to model breaking wave loads, the distribution of wave impact pressure and the associated wave kinematics during the wave impact are not yet fully understood. There are uncertainties related to the wave impact pressure distribution and the corresponding velocity components. Moreover, the role of the shape of a wave at breaking and during the interaction with structures on determining wave impact pressure and force characteristics so far remain unexplored as it involves several physical parameters.

The main purpose of the present paper is to numerically investigate the wave impact pressure on a vertical cylinder and the associated kinematics for different impact conditions, incident wave characteristics and breaker types. Based on the results from previous studies, three prominent wave impact conditions are considered in the present investigation: (1) the wave with a vertical front breaks exactly at the cylinder, (2) the broken wave hits the cylinder with a moderately overturning wave crest, and (3) the broken wave impacts the cylinder with a fully developed overturning wave crest. Two breaker types are considered in the present study; spilling and plunging breakers. Numerical experiments are performed in the three-dimensional (3D) open-source numerical wave tank REEF3D (Bihs et al., 2016*a*). The performance of the numerical model is thoroughly evaluated by comparing the numerical results with experimental data by Chakrabarti et al. (1997) and Arntsen et al. (2011). The comparisons show good agreement with the experimental data for both the wave surface elevation and the wave characteristics at breaking and the breaking wave forces. Further, the study attempts to explore new aspects related to the breaking wave-structure interaction problem.

In comparison to previous studies, the present investigation exclusively focuses on examining the influence of wave characteristics, wave impact conditions and breaker types on the wave impact pressure, kinematics and wave forces. First, the time and spatial development of the wave impact pressure and kinematics during the wave impact are analyzed. This provides more information regarding the changes in the local flow field around the cylinder. A total of 9 two-dimensional (2D) simulations are carried out to identify the breaking location and evaluate the wave characteristics for spilling and plunging breakers. Then, the breaking wave and geometric properties are evaluated in order to obtain the shape of the impacting wave for different breaker types. The localized impact phenomenon is further investigated by assessing the vertical and longitudinal variation of the flow variables around the cylinder for different impact conditions and breaker types. With a total of 27 3D simulations, the breaking wave interaction with a vertical cylinder is investigated for three impact conditions and nine different offshore wave steepnesses. The deformation and the topology changes of the free surface during the breaking process and the wave impact, where a violent wave transformation occurs, are presented and discussed. Particularly, the computed breaking wave force, impact pressure and wave kinematics are correlated with the simulated free surface deformations along with the computed breaking wave characteristics and geometric properties.

2 Numerical Model

In the present study, the open-source hydrodynamics model REEF3D (Bihs et al., 2016*a*; Bihs and Kamath, 2017) is used to simulate breaking waves and the interaction with a slender vertical cylinder. The numerical model has been extensively validated for simulating spilling and plunging breakers over slopes (Alagan Chella et al., 2015a, 2016), wave breaking over a submerged reef (Alagan Chella et al., 2015b) and breaking wave forces on slender cylinders (Kamath et al., 2016; Bihs et al., 2016*b*; Alagan Chella et al., 2017). The two-phase viscous flow is described by solving the incompressible RANS-equations together with the continuity equation that represent the conservation of the momentum and mass, respectively:

$$\frac{\partial u_i}{\partial x_i} = 0 \tag{1}$$

$$\frac{\partial u_i}{\partial t} + u_j \frac{\partial u_i}{\partial x_j} = -\frac{1}{\rho}\frac{\partial p}{\partial x_i} + \frac{\partial}{\partial x_j}\left[(\nu + \nu_t)\left(\frac{\partial u_i}{\partial x_j} + \frac{\partial u_j}{\partial x_i}\right)\right] + g_i \tag{2}$$

Here, u is the velocity averaged over time t, ρ is the fluid density, p is the pressure, ν is the kinematic viscosity, ν_t is the eddy viscosity, and g is the gravity term. The fifth-order weighted essentially non-oscillatory (WENO) scheme is employed for the discretization of the convective terms in the RANS-equations (Jiang and Shu, 1996). This higher-order scheme assures stable and oscillation-free numerical solutions without artificial damping.

For the temporal discretization, the third-order accurate TVD Runge-Kutta scheme is used (Shu and Osher, 1988). In order to perform more efficient parallel computations without affecting the numerical accuracy and stability, an adaptive time-stepping algorithm (Griebel et al., 1998) is employed. For each iteration, the simulation time step is regulated according to the CFL criterion and it is 0.1 for the present simulation cases, see Bihs et al. (2016*a*) for details. The pressure is modeled with the projection method (Chorin, 1968) leading to a Poisson equation as follows:

$$-\frac{\partial}{\partial x_i}\left(\frac{1}{\rho\left(\phi^n\right)}\frac{\partial p}{\partial x_i}\right) = -\frac{1}{\Delta t}\frac{\partial U_i^*}{\partial x_i} \tag{3}$$

The equation is solved with HYRPE's geometric multigrid PFMG (Ashby and Falgout, 1996) preconditioned BiCGStab solver (Falgout et al., 2006). In the next step, the velocity field is updated with the corrected pressure, making it divergence free:

$$u_i^{n+1} = u_i^* - \frac{\Delta t}{\rho\left(\phi^n\right)} \frac{\partial p}{\partial x_i} \tag{4}$$

The staggered grid arrangement is employed in the model to avoid spurious oscillations in the numerical solution for the pressure and velocity.

The modeling of the free surface dynamics during the breaking process is highly demanding due to the complex non-linear interactions at the interface of air and water. Another challenge is that the difference in the density and viscosity of the two phases can lead to numerical instabilities due to viscosity and density jumps at the interface. The level set method is employed to capture the free surface deformation. The thickness of a transition region is 2ϵ, where ϵ=2.1dx. The two equation $k-\omega$ model (Wilcox, 1994) is employed for turbulence modeling.

The wave generation in the numerical wave tank is based on a relaxation method proposed by Larsen and Dancy (1983) and Jacobsen et al. (2012). A part of the wave tank is considered for the wave generation at the inlet and the wave absorption at the outlet is based on the active absorption method (Schäffer and Klopman, 2000). The theoretical values are prescribed at the inlet to modulate the computational solution for the free surface elevation and velocity with a relaxation function in the relaxation zone (Jacobsen et al., 2012). A detailed analysis of different wave generation and absorption methods is presented in Miquel et al. (2018). Wave forces on the structure are calculated directly by integrating the pressure p and the normal component of the viscous stress tensor τ over the surface of the structure as given below:

$$F = \int_{\Omega} (-\mathbf{n}p + \mathbf{n}.\tau) d\Omega \tag{5}$$

where $\mathbf{n}$ is the unit normal vector to the surface and Ω is the surface of the structure. Solid boundaries are represented using a 3D ghost cell immersed boundary method (Berthelsen and Faltinsen, 2008). For more detailed information on the numerical model, refer to Bihs et al. (2016*a*).

3 Validation of numerical model

First, a grid refinement study is performed in order to make sure that the computed results are independent of the grid size. Then, the numerical results are compared against the measured data by Chakrabarti et al. (1997) in order to assess the performance of the model for simulating wave surface elevation at breaking and total breaking wave forces. The numerical wave tank is 30m long, 0.40m wide and 2.0m high with a water depth of 1.01m. A submerged 1/50 slope is installed at a distance of 12.27m from the wave inlet and followed by a flat bed extended until the end of the tank as shown in Fig. 1. A cylinder of diameter D=0.046m is placed over the flatbed at a distance of 25.68m from the wave inlet. The fifth-order Stokes wave theory (Fenton, 1999) is used to generate the waves in the numerical wave tank.

3.1 Grid refinement study for free surface elevation and total breaking wave force

Numerical simulations are performed for the three different grid sizes dx=0.01m, 0015m, 0.02m, and the results are compared with experimental data. Fig. 2 shows the comparison of the experimental

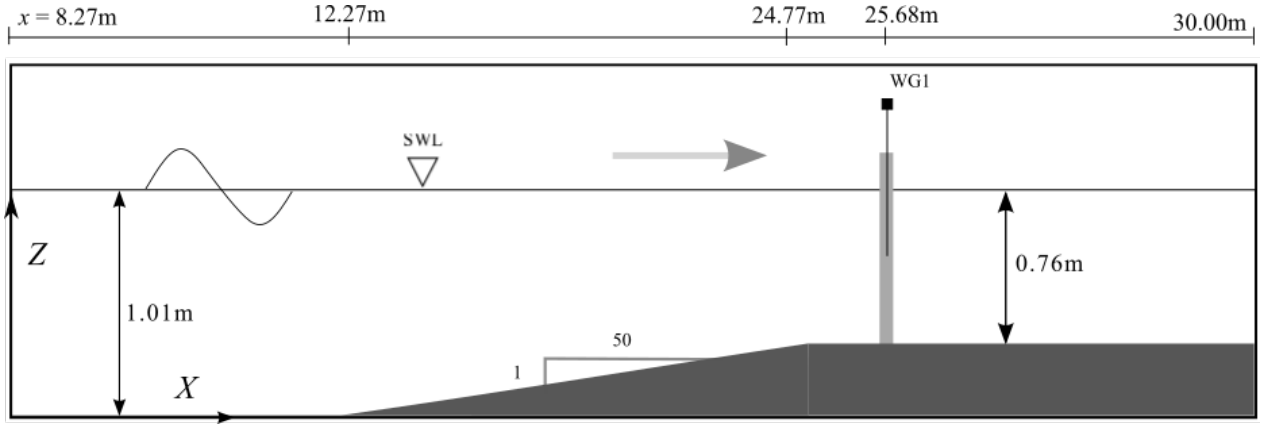

Figure 1: Numerical set-up for the laboratory conditions reported by Chakrabarti et al. (1997).

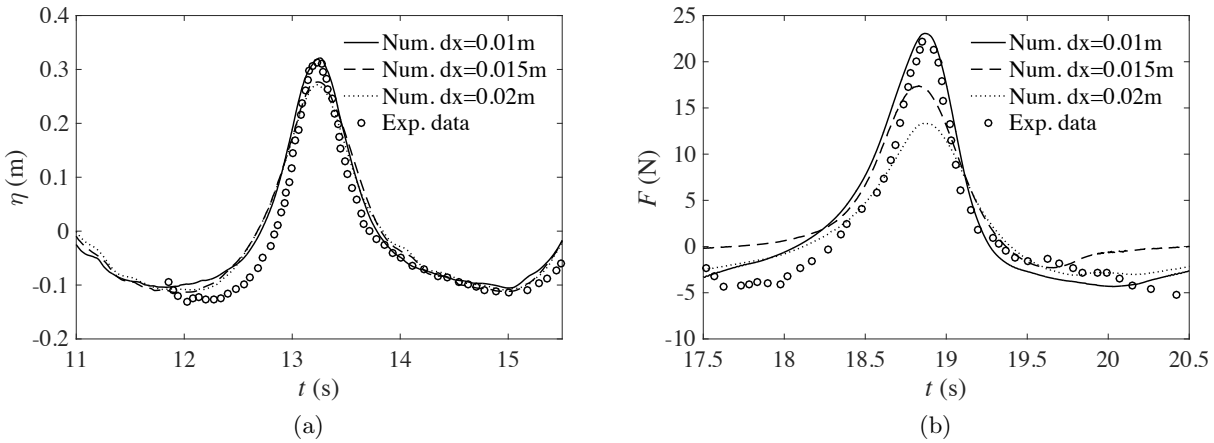

Figure 2: Comparison of numerical results for dx=0.01m, 0.015m and 0.02m and experimental data for (a) wave surface elevation at breaking (WG 1) and (b) breaking wave force on the cylinder.

data (Chakrabarti et al., 1997) and the computed results for (a) wave surface elevation at breaking, and (b) total breaking wave forces on the cylinder for different grid sizes for one wave component. The computed peak wave surface elevation is very close to the measured one for all grid sizes, but they are 13%, 11.4% lower and 1.8% higher than the experimental data for the grid sizes dx=0.02m, 0.015m and 0.01m, respectively, while the computed peak forces are 40%, 22% lower and 3.1% higher than the measured peak forces. The differences in the wave forces for coarser grids are larger due to that the wave kinematics under the wave crest are not represented correctly. With the refined grid size dx=0.01m, the free surface elevation and the computed forces are in good agreement with the experimental data. Thus, the grid size dx=0.01m is selected for all further simulations.

Next, modeling of the total breaking wave force on a vertical cylinder is validated against the experimental measurements by Chakrabarti et al. (1997) for the whole time series. The computational domain is discretized with 13.6 million uniform cells. The free surface elevation beside the cylinder at WG1 (Fig. 1) and the total breaking wave force were measured in the experiments. Figs. 3 and 4

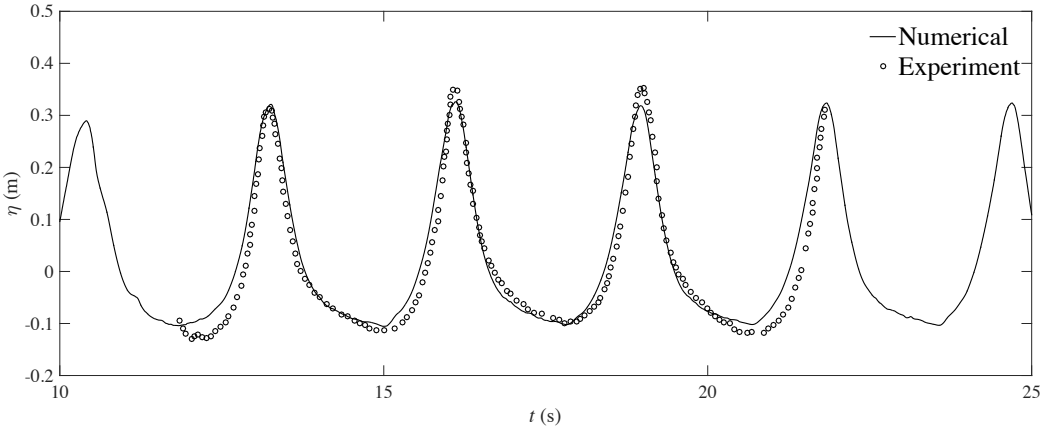

Figure 3: Comparison between numerical results for dx=0.01m and experimental data by Chakrabarti et al. (1997) for wave surface elevation (η).

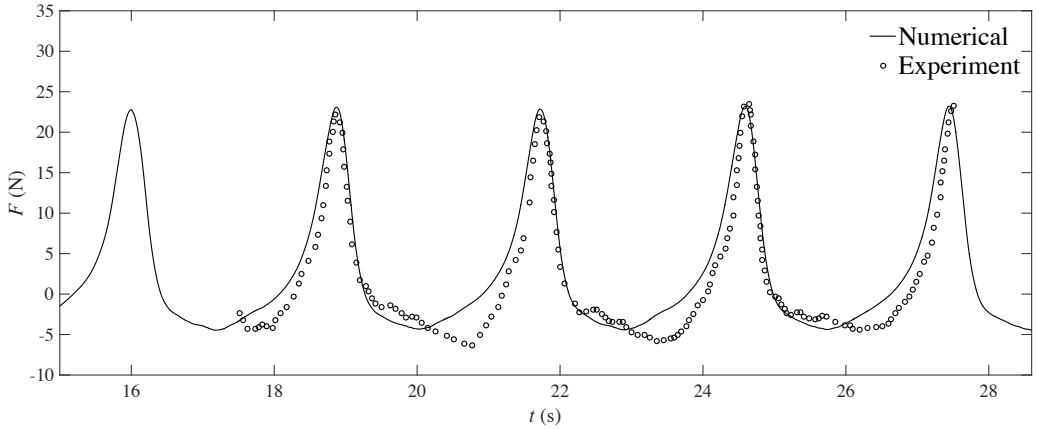

Figure 4: Comparison between numerical results for dx=0.01m and experimental data by Chakrabarti et al. (1997) for total breaking wave force (F).

show the comparison between the simulated results and measured data by Chakrabarti et al. (1997) for the free surface elevation at WG1 and the total breaking wave force (Fig. 1) for dx=0.01m. It is noticed that the simulated wave surface elevations match well with the measured data, but the simulated wave crests from t=15s to 20s are 6% lower than the experimental data. However, the wave troughs are accurately simulated including accurate representation of phase information. In the laboratory experiments performed by Chakrabarti et al. (1997), the waves were generated in intermediate water depth and the slope was placed in such a way that the waves break at the cylinder. The numerically captured free surface profiles look like a spilling breaking wave with a small overturning wave crest. Thus, it is possible that the quasi-static force contribution might be relatively higher than the impact force contribution to the total integrated force on the cylinder. On the other hand, though the peak and the upper profile of the breaking wave force-time curve are captured accurately in the numerical simulation, the lower part of the force-time curve is slightly underestimated. Overall, the numerical results are in good agreement with the measured results.

4 Results

4.1 Breaking wave interaction with a vertical cylinder

In this section, a detailed analysis is carried out concerning the vertical distribution, time and spatial development of wave impact pressure and kinematics during the wave impact event. The modeling of the breaking wave impact problem solely depends on the accurate representation of the breaking wave characteristics, wave celerity at breaking and the free surface deformation during the impact. These parameters are investigated numerically in detail for four different experimental cases reported by Arntsen et al. (2011), The computational set-up consists of a numerical wave tank of 18.65m length, 0.5m width and 1.80m height with a water depth of 0.9m, which resembles the experimental conditions reported by Arntsen et al. (2011). A 1/9.1 submerged slope is fixed at a distance of 9.3m away from the wave inlet and it is connected with a 1/50 slope and a flat bed prolonged until the end of the tank as presented in Fig. 5. On the flat bed, a cylinder of diameter D=0.06m is installed at a distance of 15.08m from the inlet. The computational domain is modeled with 12.0 million uniform cells of the grid size dx=0.01m. First, the numerical results are compared with the experimental data for the wave surface elevation at breaking and the resulting breaking wave characteristics including wave celerity and the free surface deformation during the impact.

Fig. 6 shows the comparison of computed and measured wave surface elevation at x=15.08m (WG2). In the wave tank, the wave height increases as the wave propagates over the slope, undergoing shoaling and the maximum wave height for each case occurs at the breaking point. The wave height starts to attenuate just after the breaking point and this reduction depends on the strength of the vortices generated during the complex breaking process (Basco, 1985; Miller, 1987). It appears from Fig. 6 that the measured wave surface elevations at x=15.08m are well represented in the numerical simulations. Although the computed wave crests are in good agreement with the measured data, the computed backward face of the wave troughs are not fully consistent. At x=15.08m, the waves with high velocity changes in the wave crest were already broken before hitting the cylinder. On the one hand, the breaking at this location (x=15.08m) is depth-induced breaking which is the combination of shoaling and breaking and the waves experience longitudinal and vertical deformation as they advance the cylinder. On the other hand, as the wave gauge is installed besides the cylinder, the resulting turbulent flow is influenced by shoaling, breaking and the cylinder interaction that includes reflection. Therefore, the computed backward face of the wave troughs were not fully consistent with the experimental data. However, the computed wave crests and wave peaks are reasonably well reproduced in the numerical simulation. For all cases, the wave height and free surface elevation at breaking are accurately represented in the numerical simulation.

Cases	case PL-1			case PL-2			case PL-3			case PL-4		
	H_0=0.24m, T=2.22s			H_0=0.219m, T=2.08s			H_0=0.24m, T=1.96s			H_0=0.226, T=1.86s		
	Exp	Num	% D	Exp	Num	% D	Exp	Num	% D	Exp	Num	% D
η_b (m)	0.198	0.190	-4.04	0.180	0.193	+7.22	0.195	0.198	+1.54	0.175	0.190	+8.57

H_b (m)	0.276	0.265	-3.98	0.249	0.241	-3.21	0.264	0.258	-2.27	0.246	0.243	-1.22
γ_b	0.83	0.80	-3.61	0.76	0.74	-2.63	0.80	0.78	-2.50	0.75	0.73	-2.67
Ω_b	1.15	1.10	-4.34	1.13	1.10	-2.63	1.10	1.08	-1.81	1.09	1.08	-0.92
C_b (m/s)	2.30	2.26	-1.74	2.20	2.24	+1.82	2.30	2.31	+0.43	2.20	2.27	+3.18

Table 1: Comparison between the numerical results and the experimental results by Arntsen et al. (2011) for breaking wave characteristics and celerity at breaking for four different experimental case.

Table 1 presents the comparison of the experimental results by Arntsen et al. (2011) with the numerical results for the wave characteristics and wave celerity at breaking. Fig. 7 shows a sketch of the cross-sectional view of the numerical wave tank and the relevant wave parameters. Waves undergo two different wave transformation processes when they propagate over a variable water depth on a slope and a constant water depth over the flat bed (from the deep water part to the shallow water part of the numerical wave tank). These processes are reasonably well represented in the numerical simulations and the wave height and free surface elevation at breaking (WG 2) are accurately computed for all cases (Fig. 6 and Table 1). At the breaking point, the crest particle velocity slightly exceeds the wave celerity due to the change in forward moving kinetic energy in the upper part of the wave crest (Peregrine et al., 1980; Cokelet, 1977). At the onset of breaking, a rapid transition of the wave characteristics and kinematics takes place and the wave transformation process is captured quite well in the numerical wave tank. Moreover, the computed breaker depth index (γ_b), breaker height index (Ω_b) and the wave celerity (C_b) at breaking are in good agreement with the experimental data for all cases.

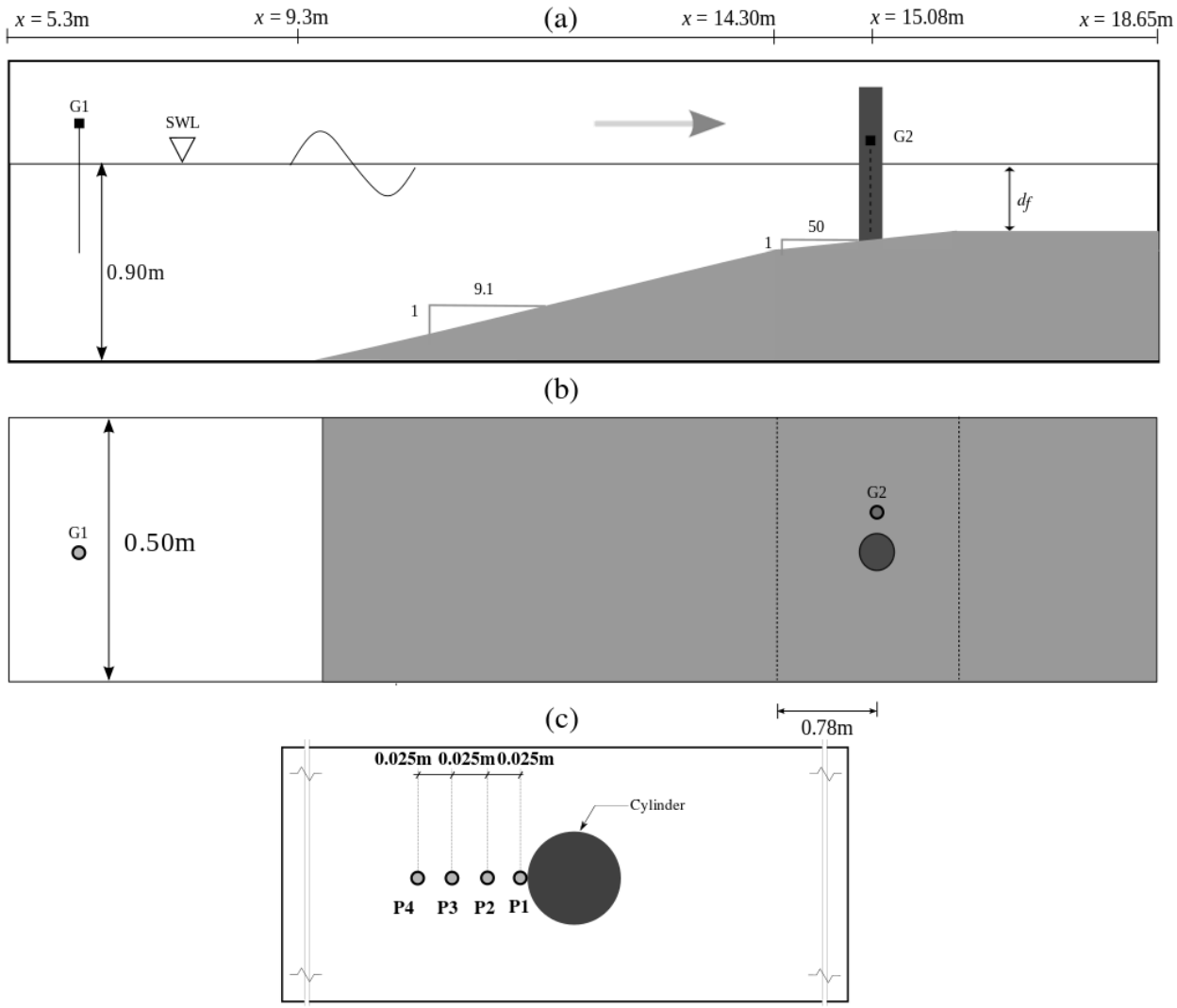

Figure 5: (a) Side view and (b) top view of numerical set-up for the laboratory conditions reported by Arntsen et al. (2011) and (c) top view of prob locations in front of the cylinder.

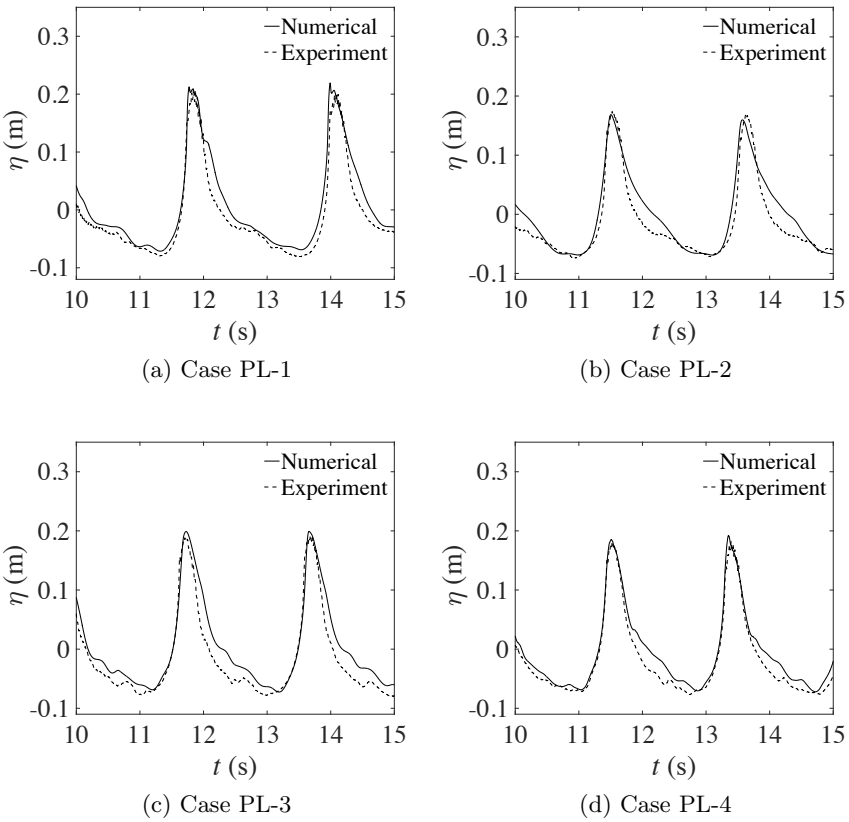

(a) Case PL-1 (b) Case PL-2

(c) Case PL-3 (d) Case PL-4

Figure 6: Comparison of numerical and experimental results by Arntsen et al. (2011) for wave surface elevation at WG 2 (x=15.08m) (Fig. 5 (b)).

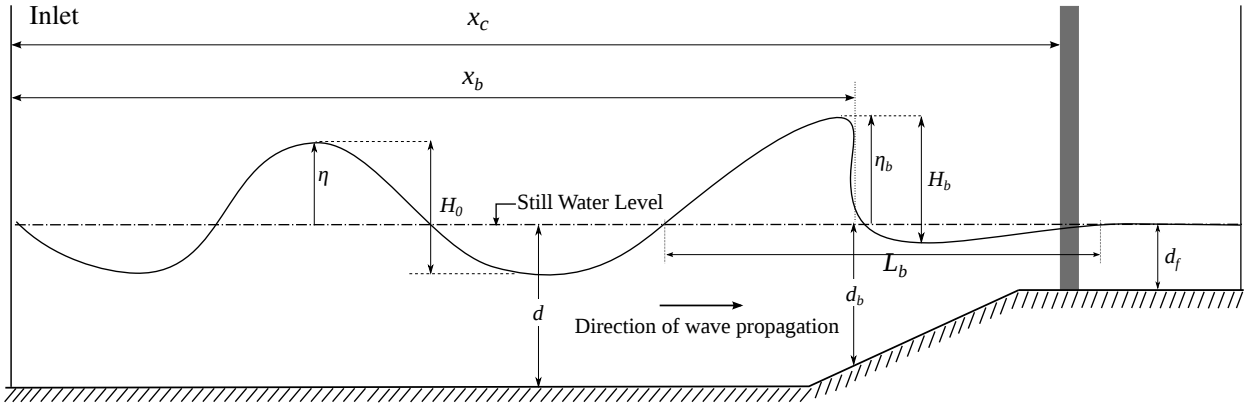

Figure 7: A sketch of cross-sectional view of the numerical wave tank and the relevant wave parameters. η_b and H_b are the wave surface elevation and wave height at breaking, X_b and X_c are the breaking location and the front face of the cylinder from the inlet, L_b and d_c are the wave length and water depth at breaking, η, H_0 and d are the wave surface elevation, wave height and water depth in the offshore region and d_f is the water depth over the flatbed portion.

4.1.1 Vertical distribution of wave impact pressure and velocity components

This section presents the vertical distribution of the maximum wave impact pressure and the velocity components (u and w) above the still water level. Here, the computed velocity components correspond to the time instant when the wave impacts the cylinder and the pressure attains its maximum value. Fig. 8 shows the computed normalized maximum wave impact pressure ($p_{max}/\rho C^2$)

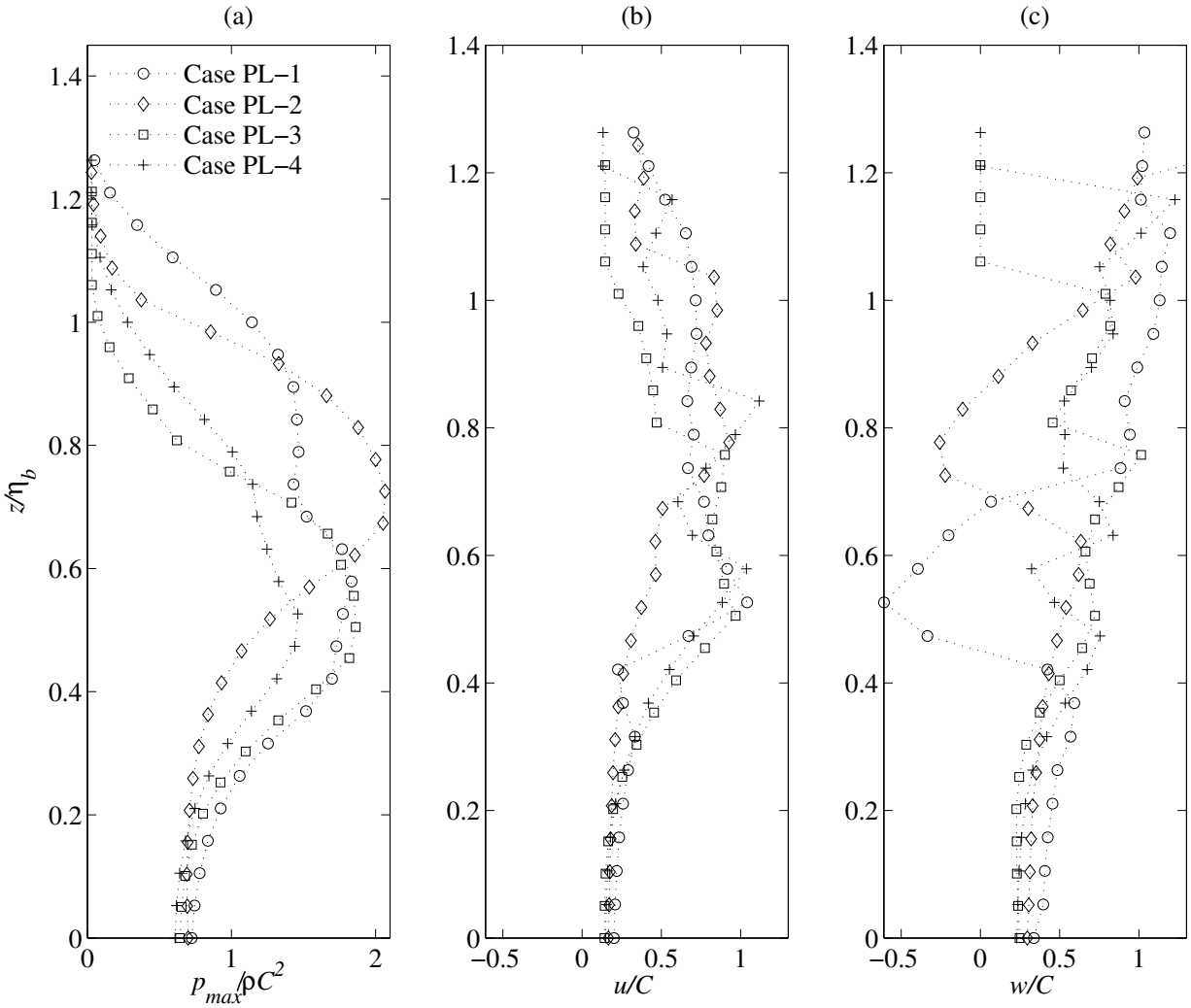

Figure 8: Computed (a) normalized wave impact pressure, (b) normalized horizontal and (c) normalized vertical components of velocities versus normalized height for cases PL-1 (H_0=0.24m, T=2.22s) , Pl-2 (H_0=0.219m, T=2.08s) , PL-3 (H_0=0.24m, T=1.96s) and PL-4 (H_0=0.226m, T=1.86s) .

and the corresponding normalized horizontal (u/C) and vertical (w/C) velocity components versus the normalized height (z/η_b) for four experimental cases. The flow quantities are computed at P1 as shown in Fig. 5 (c). The computed pressures are normalized with the stagnation pressure (ρC^2). In all four cases, the waves break in the vicinity of the cylinder and the broken waves impact the cylinder with a deformed wave crest. It appears that $p_{max}/\rho C^2$ and u/C increase as z/η_b increases

until their maximum values and then they start to decrease with further increase in z/η_b. Except for case PL-4, the u/C profile nearly follows the trend of the $p_{max}/\rho C^2$ profile (i.e. the level at which the maximum values occur for u/C and p_{max} are nearly the same) reasonably well for different impact conditions. For cases PL-1 and PL-2, w/C becomes negative during the breaking wave interaction. However, w/C increases continuously with increasing z/η_b from the still water level and reaches the maximum near the free surface for cases PL-3 and PL-4. It should be noted that upward velocity is positive and downward velocity is negative. Further, the variation of w/C in Fig. 8 (c) clearly indicates that the wave impact condition for case PL-1 and PL-2 is when the wave impacts the cylinder with a moderate overturning wave crest causing a strong wave run-up and amplifying w/C in front of the cylinder. Whereas for case PL-3 and PL-4, the wave hits the cylinder with a vertical wave front, i.e. the wave breaks at the cylinder without much wave run-up. These results are consistent with the experimental observations by Andersen et al. (2011) who showed that the breaking wave impact causes large vertical velocities in front of the cylinder compared to non-breaking or nearly breaking waves. In order to understand the variation in the w/C profile, the pressure and velocity profiles versus time will be investigated during the wave impact.

Fig. 9 presents the computed normalized wave impact pressure ($p_{max}/\rho C^2$) and the corresponding horizontal (u/C) and vertical (w/C) velocity components on the cylinder within time intervals at which the largest $p_{max}/\rho C^2$ occurs for each case, i.e. z/η_b =0.58, 0.70, 0.48 and 0.48 for cases PL-1, PL-2, PL-3 and PL-4, respectively. It appears that the largest $p_{max}/\rho C^2$ occurs for case PL-2 and the maximum u/C and w/C occur for cases PL-1 and PL-3, respectively. A snapshot of the numerically captured flow scenario during the interaction is compared with the photograph taken during the laboratory experiments as shown Fig. 10 for case PL-2. In this case, the wave interacts with the cylinder with a slightly developed overturning wave crest and this flow scenario is simulated with reasonable accuracy in the numerical wave tank.

The development of the pressure profile for each case presented in Fig. 9 (a) shows that the pressure increases rapidly with a sharp peak and it decreases slowly after attaining the maximum value. The shape and the distribution of the computed pressure profiles are also consistent with the measured pressure profiles reported by Chan et al. (1995) and Hildebrandt (2013). As can be seen from Fig. 9 (c), in contrast to the variation trend of $p_{max}/\rho C^2$ and u/C, the development of the w/C profile approaches the peak gradually with a longer rise time. After attaining the peak value, it decreases with a shorter fall time. At the onset of breaking, the wave length decreases and the local wave front steepens as the offshore wave steepness increases. As a result, a steepened wave front impacts the cylinder quickly with a shorter rise time. The computed pressure rise time is 0.011s, 0.0097s, 0.0090s and 0.0085s for cases PL-1, PL-2, PL-3 and PL-4, respectively. Therefore, the computed results suggest that the slope of the local wave front influences the pressure rise time. The flow scenario is depicted in Fig. 11 for case PL-2 with the numerically simulated free surface deformation showing the velocity magnitude. In this case, the wave breaks ahead of the cylinder (Fig. 11 (a)) and as the wave propagates further, a forward overturning wave front evolves from the wave crest (Fig. 11 (b)). Finally, the wave with a moderate overturning wave crest impinges on the cylinder leading to a separation of the wave crest behind the cylinder in the shadow region (Figs. 11 (c) and (d)). Though the height of the overturning wave crest decreases continuously shoreward, the velocity at the tip of the separated wave fronts increases until they impact the forward wave trough. It is evident that the velocity magnitude in that region (Fig. 11 (d)) is slightly higher than the velocity of the wave crest at breaking (Fig. 11 (a)). The simulated results indicate that the vertical distribution of the wave impact pressure and the associated kinematics depend largely on the location of the breaking point with respect to the structure, i.e. the wave impact conditions.

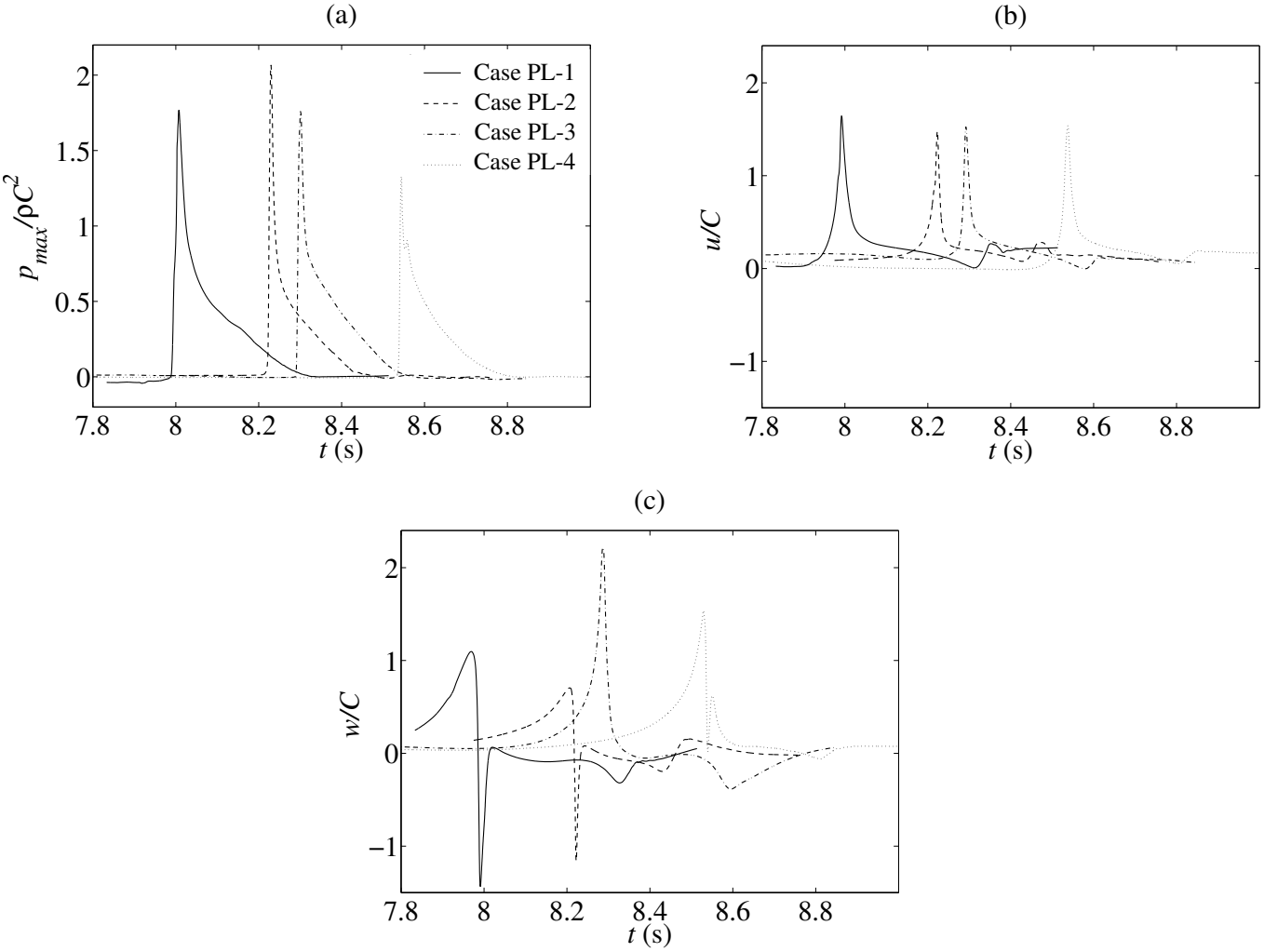

Figure 9: Computed (a) normalized wave impact pressures, (b) normalized horizontal and (c) normalized vertical velocity components versus time for four experimental cases.

This will be investigated further in Section 4.2.

4.1.2 Spatial evolution of wave impact pressure and velocity components

In this section, the evolution of the vertical profile for the wave impact pressure and the associated velocity components in space is investigated during the impact. The vertical profile of flow quantities are tracked spatially with four probe lines (P1 to P4) along the centerline and ahead of the cylinder as shown in Fig. 5 (c). The relative distance is x_w/L_b, where x_w is the distance between a given location in the wave tank and the surface of the cylinder. The probe lines are 0.025m apart which spans a distance of 0.075m and the corresponding relative distances (x_w/L_b) are 0.002, 0.009, 0.015 and 0.021 for case PL-2. In fact, the distance is 1% of L_0 and 2.2% of the wave length at breaking (L_b), implying that most variations in the wave impact pressure occur in a very short

(a) (b)

Figure 10: Comparison of (a) experiment by Arntsen et al. (2011) and (b) numerically simulated free surface profile during the breaking wave impact for case PL-2.

distance in front of the cylinder.

Fig. 12 shows the numerical spatial evolution of the normalized maximum pressure ($p_{max}/\rho C^2$) and the corresponding normalized horizontal (u/C) and vertical (w/C) velocity components versus the normalized height (z/η_b) at x_w/L_b=0.002, 0.009, 0.015 and 0.021 for case PL-2. For the $p_{max}/\rho C^2$ vertical profile, a small peak initiates at x_w/L_b=0.009 and z/η_b=0.68 and attains the maximum pressure at x_w/L_b=0.002 and z/η_b=0.74. It appears that the peak of $p_{max}/\rho C^2$ increases and the vertical profile becomes wider as the relative distance (x_w/L_b) decreases. At the same time, the maximum u/C diminishes and w/C increases as x_w/L_b decreases.

Figs. 13 and 14 show the simulated variation of horizontal and vertical velocity components, respectively, during the wave impact for case PL-2. Along the longitudinal center line of the cylinder while the broken wave advances the cylinder, u/C decreases (Fig. 13) due to the temporary retardation of the flow in front of the cylinder, while w/C increases (Fig. 14) due to a rise in water level in front of the cylinder. As can be observed in Fig. 14 (a) to (d), the vertical velocity component w/C reaches its maximum value when the overturning wave crest hits the cylinder. Then, w/C decreases behind the cylinder as the deformed wave crest propagates farther downstream as depicted in Fig. 14 (e) and (h). It is noticed that the vertical velocity component of the downstream water jet that emerged behind the cylinder (Fig. 14 (g) and (h)) is higher than the one at the wave crest at breaking. Most prominent spatial changes in the flow characteristics take place within a fraction of the wave length at breaking (L_b) very close to the cylinder. The computed pressure and velocity profiles clearly indicate that the breaking wave impact event is a highly localized phenomenon which is strongly influenced by local flow conditions.

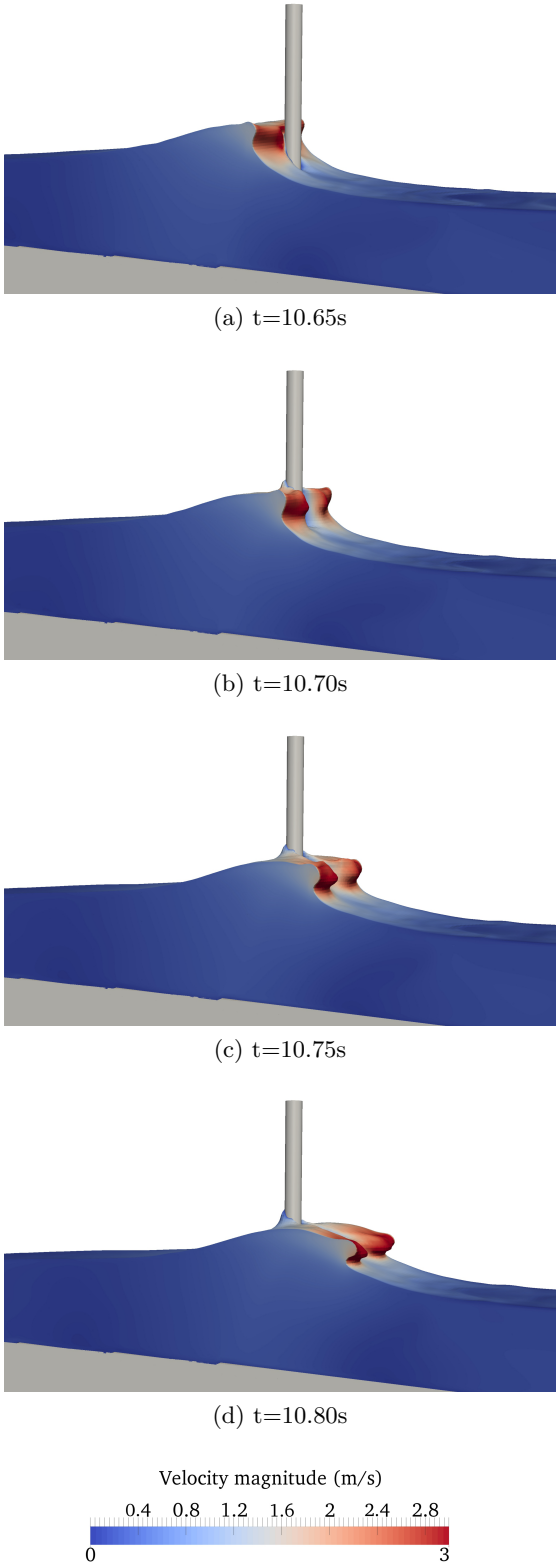

(a) t=10.65s

(b) t=10.70s

(c) t=10.75s

(d) t=10.80s

Figure 11: Simulated free flow features during the breaking wave interaction at t=(a) 10.65s, (b) 10.70s and (c) 10.75s and (d) 10.80s for case PL-2.

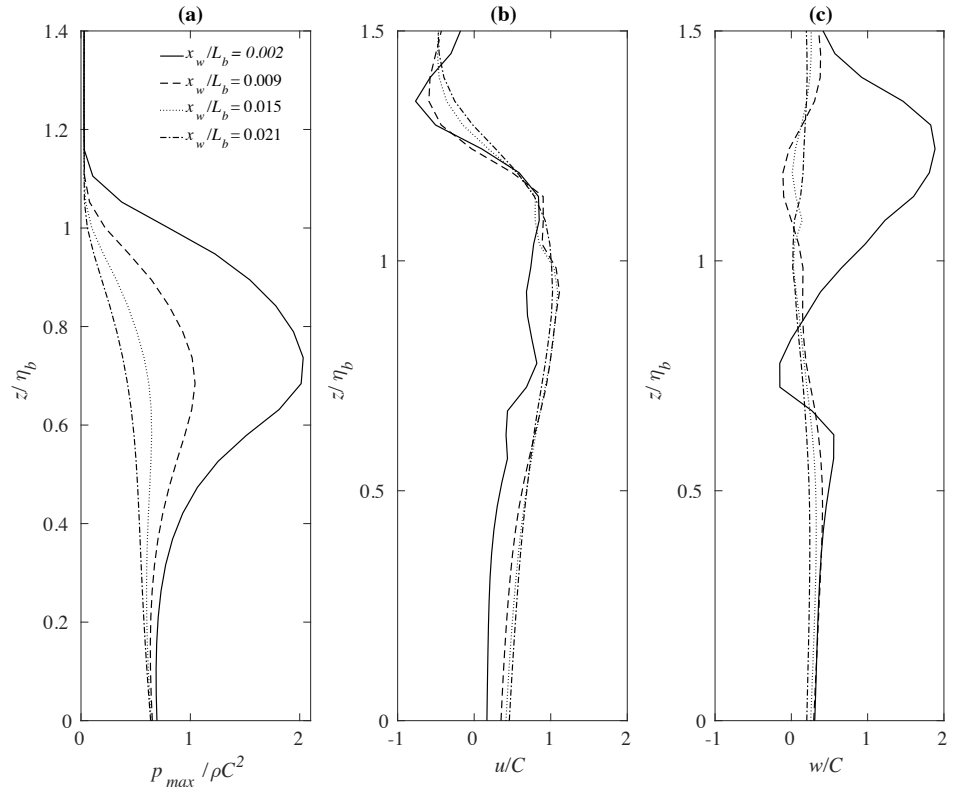

Figure 12: Spatial evolution of computed normalized (a) wave impact pressure, (b) horizontal and (c) vertical velocity components versus normalized height (z/η_b) for case PL-2 at x_w/L_b=0.002, 0.009, 0.0015 and 0.021.

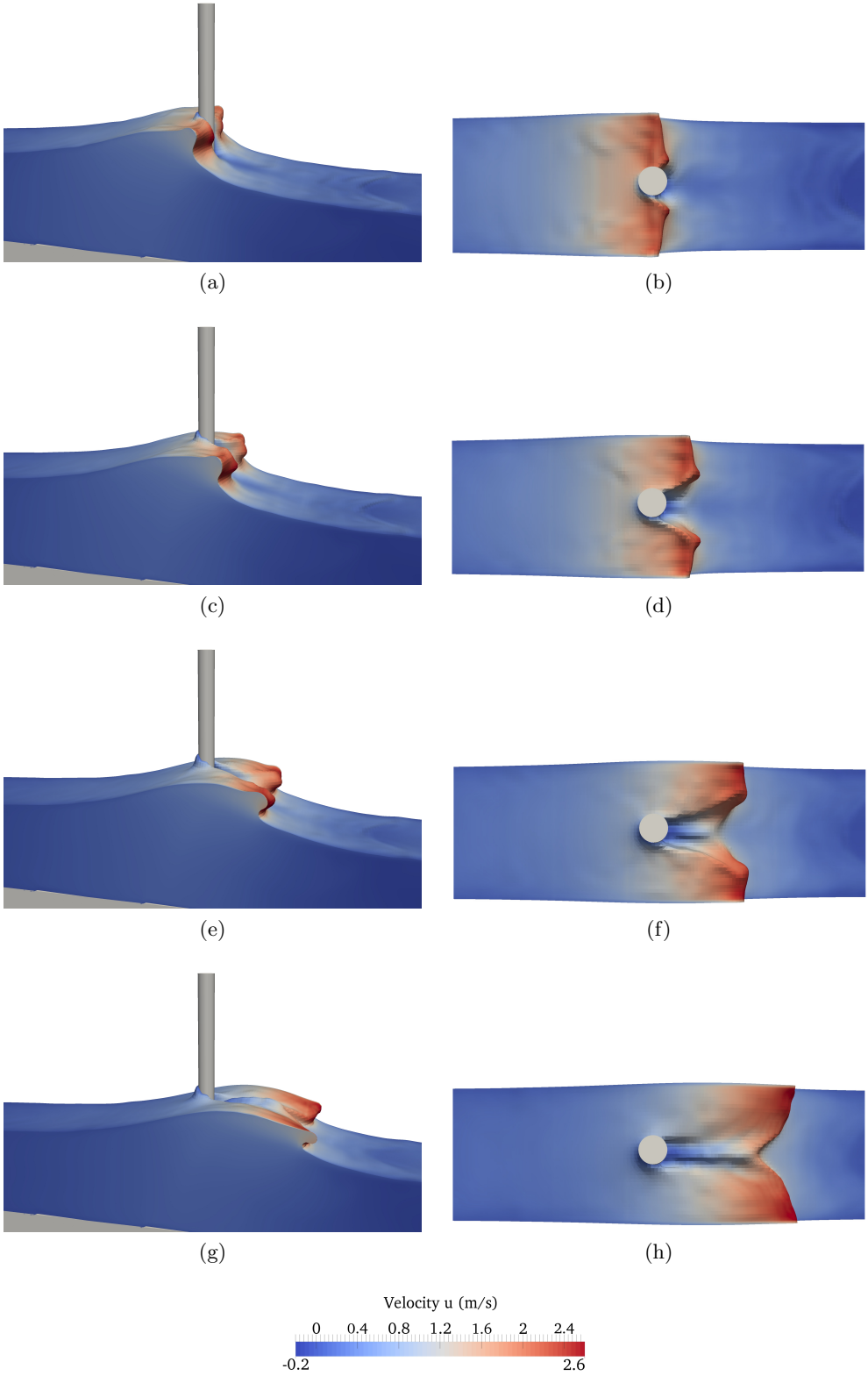

Figure 13: Simulated variation of horizontal velocity (u) component at t=10.68s, 10.72s, 10.78 and 10.84s for case PL-2.

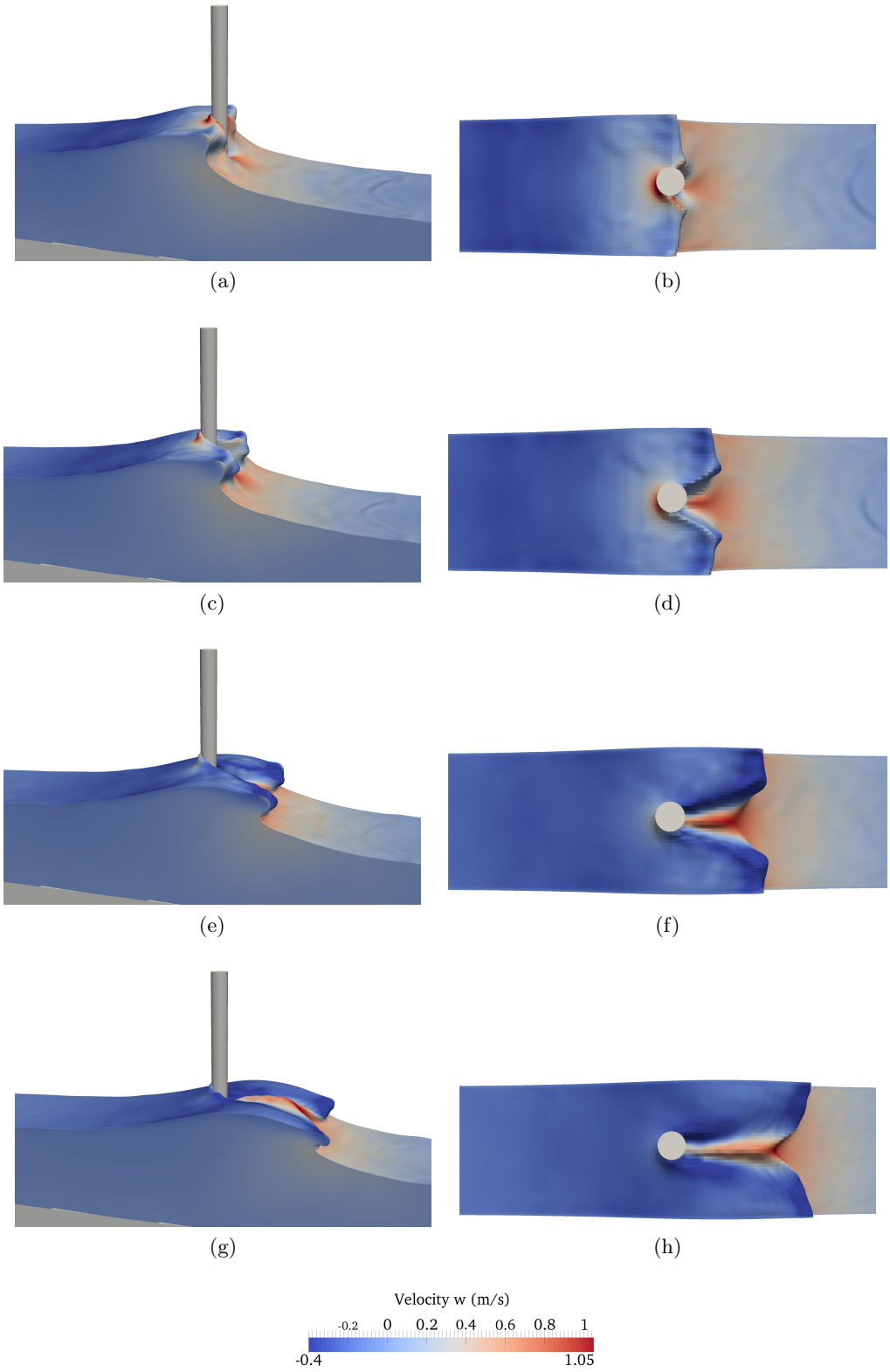

Figure 14: Simulated variation of vertical velocity (w) component at t=10.68s, 10.72s, 10.78 and 10.84s for case PL-2.

Further, the time profiles for pressure and velocity components at z/η_b=0.74 (where the largest $p_{max}/\rho C^2$ occurs) are presented in Fig. 15. In this case, the wave breaks slightly ahead of the cylinder and interacts with a moderately developed overturning wave crest.

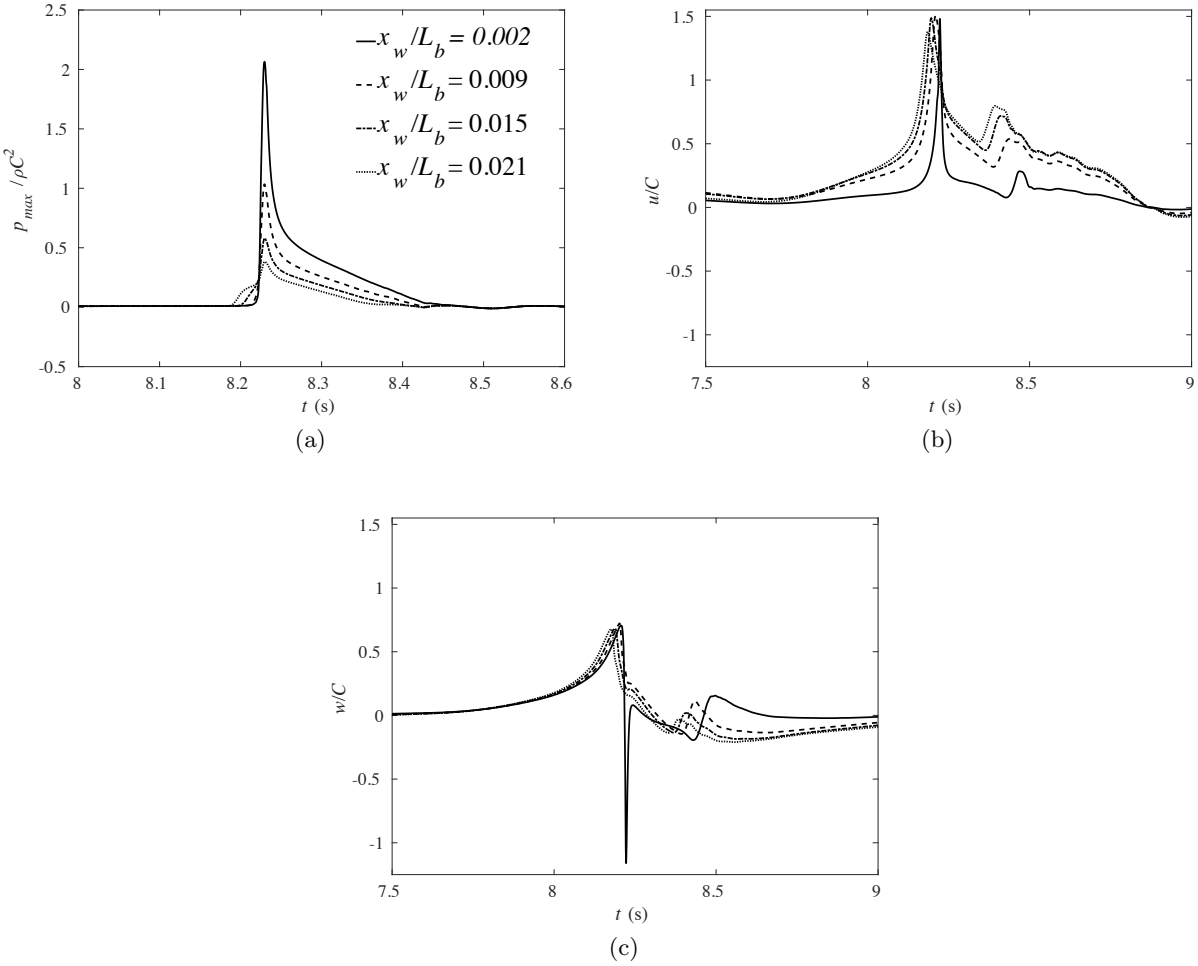

Figure 15: Computed normalized (a) wave impact pressure, (b) horizontal and (c) vertical velocity components versus time for case PL-2.

As the broken wave approaches the cylinder further, the $p_{max}/\rho C^2$ profile becomes higher and wider. It appears that $p_{max}/\rho C^2$ reaches its maximum value just in front of the cylinder and it is 2.0 times and 5.5 times the pressure at x_w/L_b=0.009 and 0.021, respectively. A secondary peak appears after the primary peak and its value decreases for u/C and increases for w/C. At x_w/L_b=0.021, u/C is 9% and w/C is 6% higher than their maximum values.

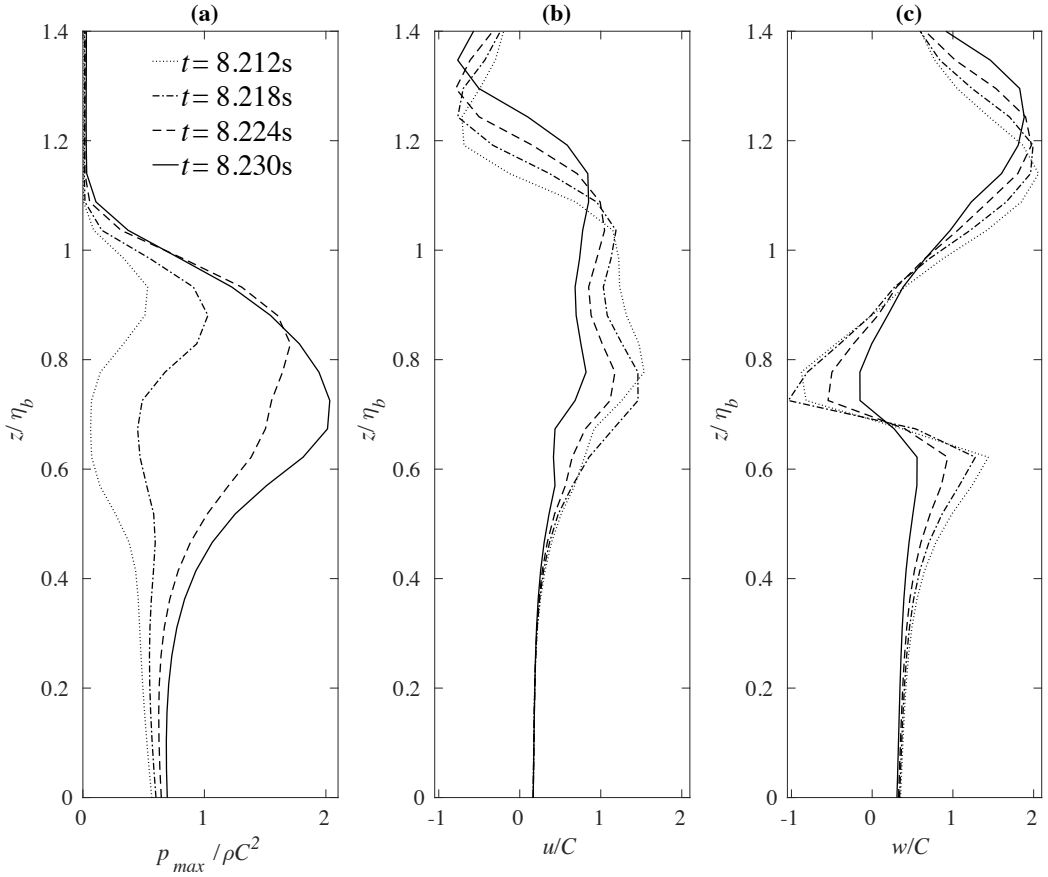

Figure 16: Time evolution of computed normalized (a) wave impact pressure, (b) horizontal and (c) vertical velocity components at t= 8.212s, 8.218s, 8.224s and 8.230 for case PL-2.

Unlike the $p_{max}/\rho C^2$ profile, the u/C profile becomes narrower and sharper as x_w/L_b decreases. In this case, w/C attains its maximum value at 8.20s followed by u/C at 8.215s and then, $p_{max}/\rho C^2$ at 8.23s. At the breaking wave impact (x_w/L_b=0.002), a sudden negative peak appears right after w/C reaching the positive peak. The reason might be due to the impact of the breaking wave with an overturning wave crest with the downward velocity in front of the cylinder. The results imply that the pressure and the vertical velocity component tend to be more sensitive to the spatial variation during the impact in the vicinity of the cylinder than the horizontal velocity component. This can be explained by that potential energy turns into kinetic energy after breaking and then, as the wave motion is obstructed by the presence of the cylinder, the kinetic energy is converted into dynamic pressure. As a result, the horizontal velocity decreases and the vertical velocity increases due to a rise in the mean water level in front of the cylinder due to wave run-up as depicted Figs. 13 and 14.

4.1.3 Time evolution of wave impact pressure and velocity components

This section investigates the sensitivity of the wave impact pressure for small changes in time. The time evolution of the vertical flow quantity profiles are investigated for four time steps consecutively at the interval of 0.006s before the time of the wave impact (x_w/L_b=0.002). Fig. 16 shows the time evolution of the computed normalized pressure ($p_{max}/\rho C^2$) and the corresponding normalized horizontal and vertical velocity components versus the normalized depth (z/η_b) for t=8.212s, 8.218s, 8.224s and 8.230s for case PL-2. As mentioned in Section 4.1.2, the wave breaks ahead of the cylinder and it impacts the cylinder with a moderately evolved overturning crest and the maximum $p_{max}/\rho C^2$ occurs at z/η_b=0.74. Initially, the pressure under the wave crest is lower than the pressure at the still water level i.e. hydrostatic pressure, where a small peak appears at z/η_b=0.93. Meanwhile u/C and w/C attain their maximum positive values at z/η_b=0.77 and 1.14, respectively. As the time increases further, $p_{max}/\rho C^2$ increases and its peak shifts downwards. The positive peak value of u/C decreases without much change in the vertical position (z/η_b=0.77). Similarly, w/C decreases but the peak moves upward (z/η_b=1.25). However, the w/C profile has the maximum negative peak at z/η_b=0.72 and the positive peak at z/η_b=1.25, but as the time increases, the negative peak increases and the positive peak decreases as shown in Fig. 16 (c).

A double positive peak for the u/C profile (Fig. 16 (b)) and a positive and a negative peak for the w/C profile (Fig. 16 (c)) denote the upper and lower part of the forward curling wave crest. During a few time steps before the wave impacts the cylinder, the wave with a steep wave front propagates faster and higher. As the deformed wave crest overturns further after breaking (Figs. 13 (a) and (b) and 14 (a) and (b)), the wave height decreases shoreward. Here, the transformation of kinetic energy to pressure takes place and thus, $p_{max}/\rho C^2$ increases rapidly and u/C and w/C decrease moderately. The computed time development profiles of $p_{max}/\rho C^2$ suggest that steep pressure gradients can be expected in a short time interval (order of 0.005s) during the wave impact. In fact, the maximum pressure occurs near the center of the forward overturning wave crest (z= 0.26 z/η_b below it). Moreover, the vertical distributions of flow variables primarily depend on the wave impact condition and this will be investigated further in the following sections.

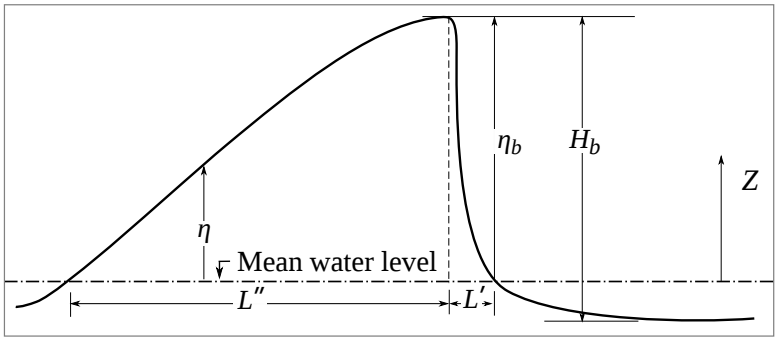

Figure 17: A sketch of wave profile at breaking and the relevant geometrical parameters.

4.2 Wave impact pressures and kinematics during the breaking wave interaction with a cylinder for plunging and spilling breaking waves

This section consists of four parts. The first part (Section 4.2.1) examines the breaking wave characteristics and geometric properties for nine different offshore wave steepnesses with 2D simulations. The second part (Section 4.2.2) investigates the vertical distribution of the maximum wave impact pressure on the cylinder and the corresponding velocity components subject to three wave impact conditions for plunging and spilling breakers. The third part (Section 4.2.3) assesses the longitudinal variation of the maximum wave impact pressure and velocity components upstream and downstream of the cylinder. The fourth part (Section 4.2.4) analyses the maximum breaking wave force and wave impact pressure for different impact conditions. Numerical experiments are carried out for nine different offshore wave steepnesses (five for plunging breakers and four for spilling breakers) under three different wave impact conditions resulting in a total of 9 2D and 27 3D simulations as listed in Table 2. As mentioned in Section 1, the wave impact condition has a large influence on the wave impact pressure, kinematics and forces (Zhou et al., 1991; Chan et al., 1995; Wienke and Oumeraci, 2005; Kamath et al., 2016). This has been investigated by considering three different wave impact conditions, i.e. three different relative distances between the cylinder and the breaking point. Fig. 17 shows the wave profile at breaking and the relevant geometrical parameters. The impact conditions are simulated by changing the relative locations of the cylinder (x_c) with respect to the breaking location (x_b). The relative distance (x_r) is defined as $x_r = (x_b - x_c)/L_b$ (where x_b and x_c are the location of the breaking point and the cylinder from the inlet of the wave tank, respectively (Fig.7). The conditions are : (1) when the wave breaks exactly at the cylinder (WI-1) and x_r=0.0, (2) when the broken wave approaches the cylinder with a moderately developed overturning wave crest (WI-2) and x_r=0.09 and (3) when the broken wave with a fully developed overturning wave crest impinges the cylinder (WI-3) and x_r=0.18 as depicted in Fig. 18. These three wave impact conditions are selected as they correspond to the most prominent flow scenarios that occur during the breaking process. Two types of breakers, i.e. plunging breakers and spilling breakers, are considered in the present study.

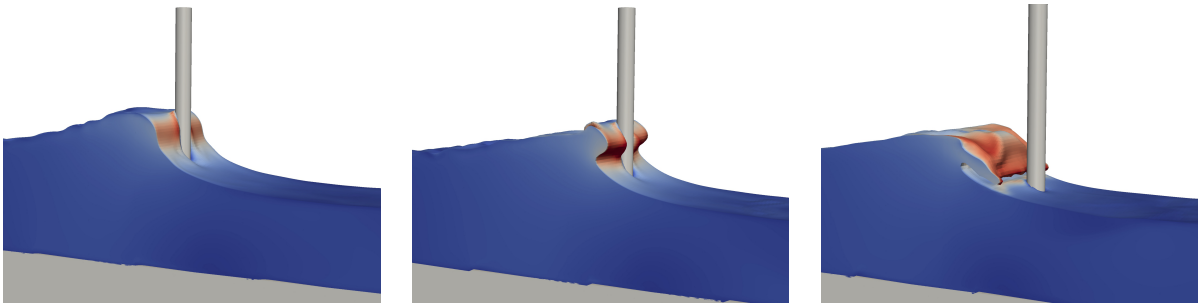

(a) WI- 1 (b) WI- 2 (c) WI- 3

Figure 18: Wave impact conditions considered in the present study : WI-1: when the wave breaks exactly on the cylinder, WI-2: when the wave breaks ahead of the cylinder and interacts with a moderately developed overturning wave crest and WI-3: when the wave breaks far before the cylinder and interacts with a fully developed overturning wave crest.

Three wave impact conditions were considered in the study comprising the interaction of the onset of breaking to fully developed overturning wave crest with a vertical cylinder. These deformed waves (breaking to broken conditions) are modeled in such a way that they impinge the cylinder before hitting the forward free surface, and the air-entrainment is avoided before the interaction. The main intention of the present study is to analyze the flow situations that yield massive wave loads on the cylinders, i.e. a rapid change in the forward momentum occurs, causing an impact force on it in a very short duration. On the other hand, air-entrainment from wave breaking and droplet impact is known to act as a layer of air cushion between the water and the structure and a slight reduction in the impact pressures is expected. This effect has been exclusively studied by Bredmose et al. (2015). The breaker types are categorized based on the relationship between the water depth in the flatbed portion next to the slope (d_f, Fig. 7 (a)) and the deep water wave height (H_0) as proposed by Yao et al. (2013):

$$d_f/H_0 < 1.80 \text{ for plunging breakers}$$
$$1.80 \leq d_f/H_0 \leq 2.80 \text{ for spilling breakers}$$
$$d_f/H_0 > 2.80 \text{ for non-breaking waves}$$

The breaker height (H_b) and the breaker water depth (d_b) as presented in Fig. 7 are the important parameters describing the local wave kinematics at the onset of breaking (Weggel, 1972; Goda, 2010). The breaker depth index (γ_b) and the breaker height index (Ω_b) are the non-dimensional parameters in terms of water depth, incident wave height and wave height at breaking. The breaker depth index ($\gamma_b = H_b/d_b$) denotes the non-dimensional wave height at breaking and becomes larger for waves that break farther shoreward at a shallower water depth. The breaker height index ($\Omega_b = H_b/H_0$) refers to how the breaker height is compared to the incident wave height. As the wave advances the breaking point, the wave profile deforms and becomes skewed in the wave propagation direction. In the present study, the geometry of the wave profile at breaking is defined using the wave steepness and asymmetry factors proposed by Kjeldsen and Myrhaug (1978) as presented in Alagan Chella et al. (2015a), defined as follows:

$$\text{Crest front steepness , } \varepsilon = \frac{\eta_b}{L'}$$

Crest rear steepness , $\delta = \frac{\eta_b}{L''}$
Horizontal asymmetry factor, $\mu = \frac{\eta_b}{H_b}$
Vertical asymmetry factor, $\lambda = \frac{L''}{L'}$

Simu. nos.	Breaker type	Simulation cases	Impact conditions	Deep water wave height, H_0 (m)	Wave period, T (s)	Breaker parameter, d_f/H_0
1	Plunging breakers, PL	PL-1	WI-1	0.240	2.22	1.38
2			WI-2			
3			WI-3			
4		PL-2	WI-1	0.219	2.08	1.50
5			WI-2			
6			WI-3			
7		PL-3	WI-1	0.240	1.96	1.37
8			WI-2			
9			WI-3			
10		PL-4	WI-1	0.216	1.86	1.46
11			WI-2			
12			WI-3			
13		PL-5	WI-1	0.260	1.66	1.27
14			WI-2			
15			WI-3			
16	Spilling breakers, SP	SP-1	WI-1	0.165	1.90	2.0
17			WI-2			
18			WI-3			
19		SP-2	WI-1	0.181	2.00	1.82
20			WI-2			
21			WI-3			
22		SP-3	WI-1	0.172	1.83	1.92
23			WI-2			
24			WI-3			
25		SP-4	WI-1	0.183	1.86	1.82
26			WI-2			
27			WI-3			

Table 2: List of simulation cases for plunging and spilling breakers.

4.2.1 Characteristics and geometrical properties

A total of 9 2D simulations are performed without the cylinder in order to determine the breaking location and calculate the characteristics and geometric properties of the breaking waves over the submerged structure for different offshore wave steepnesses. Fig. 19 shows the comparison of

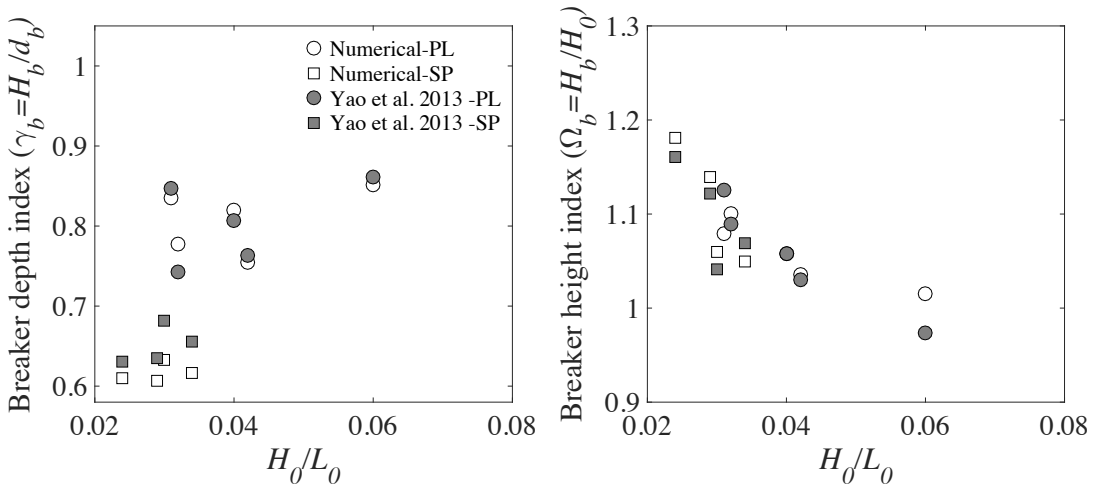

Figure 19: Computed breaker depth index (γ_b=H_b/d_b) and breaker height indiex (Ω_b=H_b/H_0) for plunging and spilling breakers for different offshore wave steepnesses. Circles: plunging breakers (PL), squares: spilling breakers (SP) and solid circles and squares: results based on Yao et al. (2013)

numerical results with the calulated values using the expression proposed by Yao et al. (2013) for the breaker depth index (γ_b) and breaker height index (Ω_b) versus the offshore wave steepnesses (H_0/L_0) for spilling and plunging breakers. It appears that γ_b increases and Ω_b decreases as the wave steepness increases for both breakers. The computed results are in good agreement with the calculated values using an expression proposed by Yao et al. (2013) based on laboratory experiments. Unlike waves on plane slopes, γ_b increases as H_0/L_0 increases since all the waves break over the flatbed next to the slope. In addition, H_b increases with increasing wave steepness. However, Ω_b follows the same trend as the wave breaking over plane slopes. Unlike plunging breakers over plane slopes, γ_b is less than 1.0 for plunging breakers in the present study and they also grow slower than the spilling breakers before reaching the breaking point. For plunging breakers, waves with higher H_0/L_0 are relatively short waves and experience lesser interaction with the seabed and they break father ashore on the flatbed when compared to waves with lower H_0/L_0.

Fig. 20 presents the crest front steepness (ε), the crest rear steepness (δ), the horizontal asymmetry factor (μ) and the vertical asymmetry factor (λ) versus offshore wave steepness (H_0/L_0) for spilling and plunging breakers. For both breakers, ε and δ increase as H_0/L_0 increases and this is also consistent with the results of wave breaking over slopes (Alagan Chella et al., 2015a, 2016). However, μ decreases slightly for spilling breakers, but in contrast to wave breaking over plane slopes, it increases significantly for plunging breakers as H_0/L_0 increases. On the other hand, λ does not change much for spilling breakers and becomes smaller for plunging breakers for waves as H_0/L_0 increases. In the case of wave breaking over slopes, λ decreases with increasing H_0/L_0 for both breakers. Therefore, as in the case of breaking wave characteristics, the geometrical properties of the wave profile at breaking over submerged structures are different from wave breaking over plane

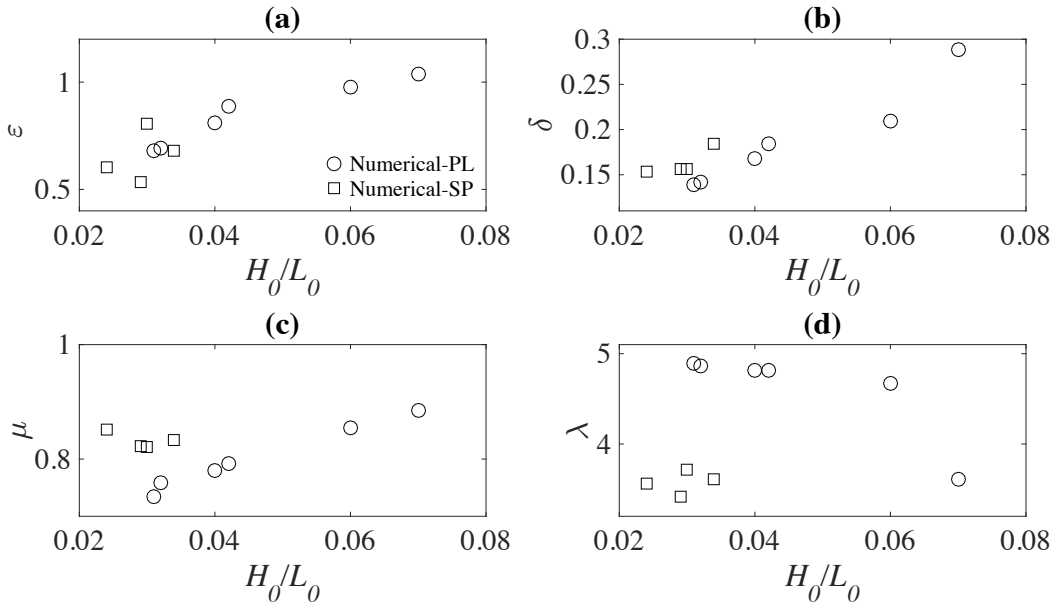

Figure 20: Computed geometric properties versus offshore wave steepness (H_0/L_0) for plunging and spilling breakers: circles: plunging breakers (PL) and squares: spilling breakers (SP).

slopes.

4.2.2 Vertical distribution of wave impact pressure and velocity components for different impact conditions

With a total of 27 3D simulations, the vertical distribution and longitudinal variation of the maximum wave impact pressure (p_{max}) and the corresponding velocity components (u and w) are investigated for plunging and spilling breaking waves. Among 27 cases, the vertical variations of the lowest (PL-1 and SP-1) and highest (PL-5 and SP-4) wave steepness cases for each breaker type are considered in order to present a concise discussion of the results.

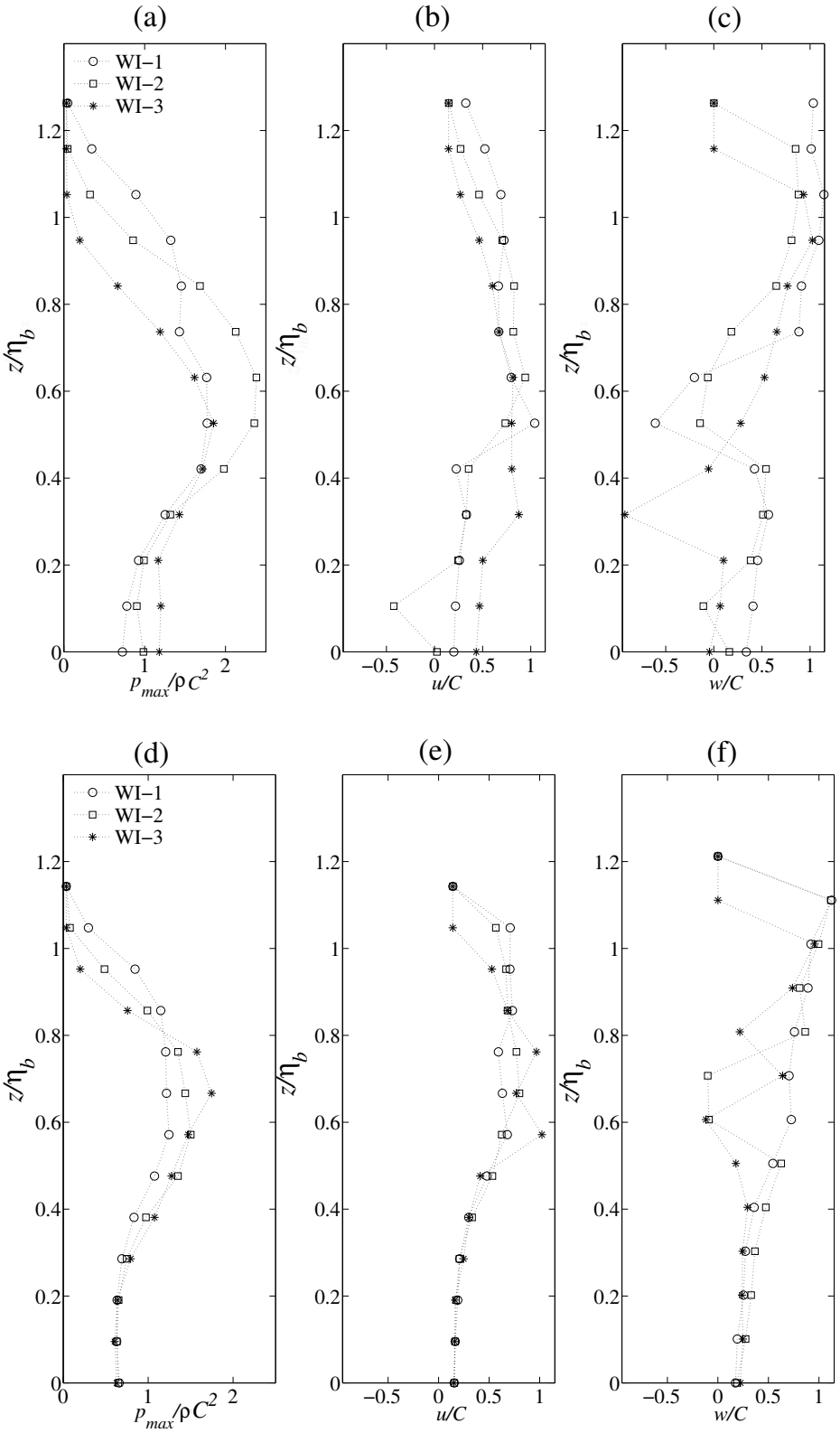

Figure 21: Computed vertical variation of normalized wave impact pressure, horizontal and vertical velocity components versus normalized height for the plunging breaker cases, PL-1 (H_0=0.24m, T=2.22s) and PL-5 (H_0=0.219m, T=2.08s) for three impact conditions, WI-1: wave breaks exactly on the cylinder, WI-2: wave breaks ahead of the cylinder and WI-3: wave breaks far before the cylinder.

Fig. 21 shows the computed vertical distribution of normalized maximum pressure ($p_{max}/\rho C^2$) and the resulting normalized horizontal (u/C) and vertical (w/C) velocity components on the cylinder versus the normalized depth for cases PL-1 and PL 5 for three wave impact conditions. The computed values are obtained at P1 above the still water level (See Fig. 5). For case PL-1 (Figs. 21 (a to c)), the largest $p_{max}/\rho C^2$ occurs when the cylinder is exposed to condition WI-2 at z/η_b=0.63 which is 28% greater than for condition WI-1. However, the largest values for u/C (z/η_b=0.53) and w/C (z/η_b=1.05) occur for condition WI-1 and they are 10% and 20%, respectively, larger than for condition WI-2. Fig. 22 presents the numerically modeled free surface flow features around the cylinder under condition WI-2 for case PL-1. When the broken wave with a moderate overturning wave crest approaches the cylinder (Fig. 22 (a)), it hits the cylinder at the wave crest level as depicted in Fig. 22 (b). In the case of PL-5 (Figs. 21 (d to f)), the cylinder experiences the largest $p_{max}/\rho C^2$ (z/η_b=0.67) and u/C (z/η_b=0.67) when the wave breaks far before the cylinder (condition WI-3) and their maximum values are 43% and 50%, respectively higher than for condition WI-2. Further, the maximum positive w/C occurs at z/η_b=1.11 for condition WI-1. The simulated free surface changes during the broken wave interaction for case PL-5 and condition WI-3 are presented in Fig. 23. Under this flow scenario, the wave breaks far ahead of the cylinder and the overturning wave crest starts to evolve as the broken wave advances towards the cylinder (Fig. 23 (a)). Finally, the broken wave with a fully developed curling wave front impinges the cylinder at the forward wave trough level as shown Fig. 23 (b). The results in Fig. 23 will be discussed further in Section 4.2.3.

Despite that the incident wave steepness of case PL-5 is greater than case PL-1, the largest $p_{max}/\rho C^2$ occurs for case PL-1, while the largest values of u/C and w/C are nearly the same for both cases irrespective of the offshore wave steepnesses. It seems possible that the wave impact condition largely influences the pressure distribution on the cylinder, but this does not affect the velocity distribution. As mentioned in Section 4.2.1, γ_b is larger and Ω_b and L_b are lower for case PL-5 than for case PL-1, corresponding to γ_b=0.83 (Fig. 19 (a)) and Ω_b=0.97 (Fig. 19 (b)). The results from the geometric analysis indicate that the wave profile at breaking for case PL-1 consists of a wider wave crest, a deeper preceding wave trough and a longer wave length at incident and at breaking when compared to case PL-5, corresponding to ε=0.68 (Fig. 20 (a)), μ=0.73 (Fig. 20 (c)) and λ=4.90 (Fig. 20 (d)). Therefore, the wave impingement of this less steep crest front is stronger than for the other two wave impact conditions. For both cases, the u/C profile follows the trend of the $p_{max}/\rho C^2$ profile, attaining its maximum value at $0.1z/\eta_b$ below the maximum $p_{max}/\rho C^2$ level. Fig. 24 shows the computed normalized maximum pressure ($p_{max}/\rho C^2$) and the associated normalized horizontal and vertical velocity components on the cylinder versus the normalized depth for cases SP-1 and SP-4 for three wave impact conditions (Fig. 18). It appears that in the case of SP-1, the largest $p_{max}/\rho C^2$ (z/η_b=0.76) and u/C (z/η_b=0.88) occur for the impact condition when the wave breaks at the cylinder (WI-3) and they are 10% and 28%, respectively, larger than for condition WI-1. The maximum w/C occurs for condition WI-1 and it is 21% higher than for condition WI-2. For SP-4 (Fig. 24 (b)), condition WI-2 (i.e. wave breaks before the cylinder) exerts the largest $p_{max}/\rho C^2$ (z/η_b=0.76) which is 30% larger than for condition WI-1. The corresponding maximum values of u/C and w/C occur at z/η_b=1.0, and they are 25% and 19%, respectively, larger than for condition WI-1.

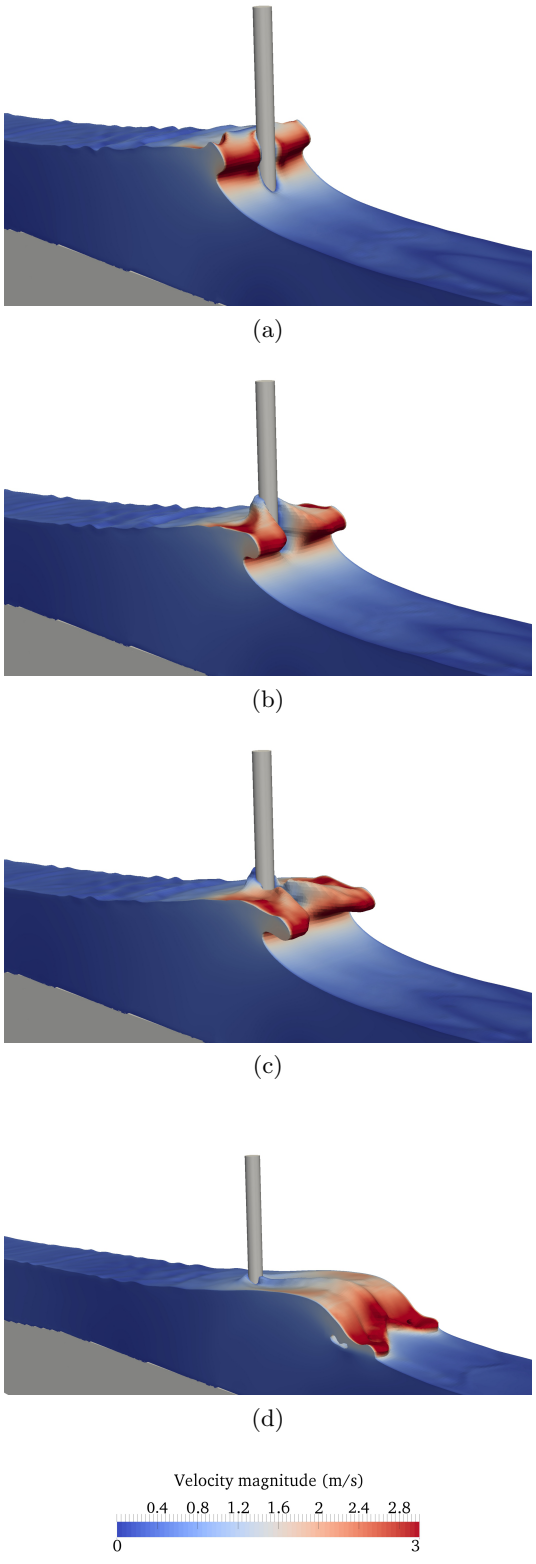

Figure 22: Simulated free surface flow features at t=10.1s, 10.2s, 10.4s and 10.8s for case PL-1 (H_0=0.24m, T=2.22s) and wave impact condition WI-2: wave breaks ahead of the cylinder

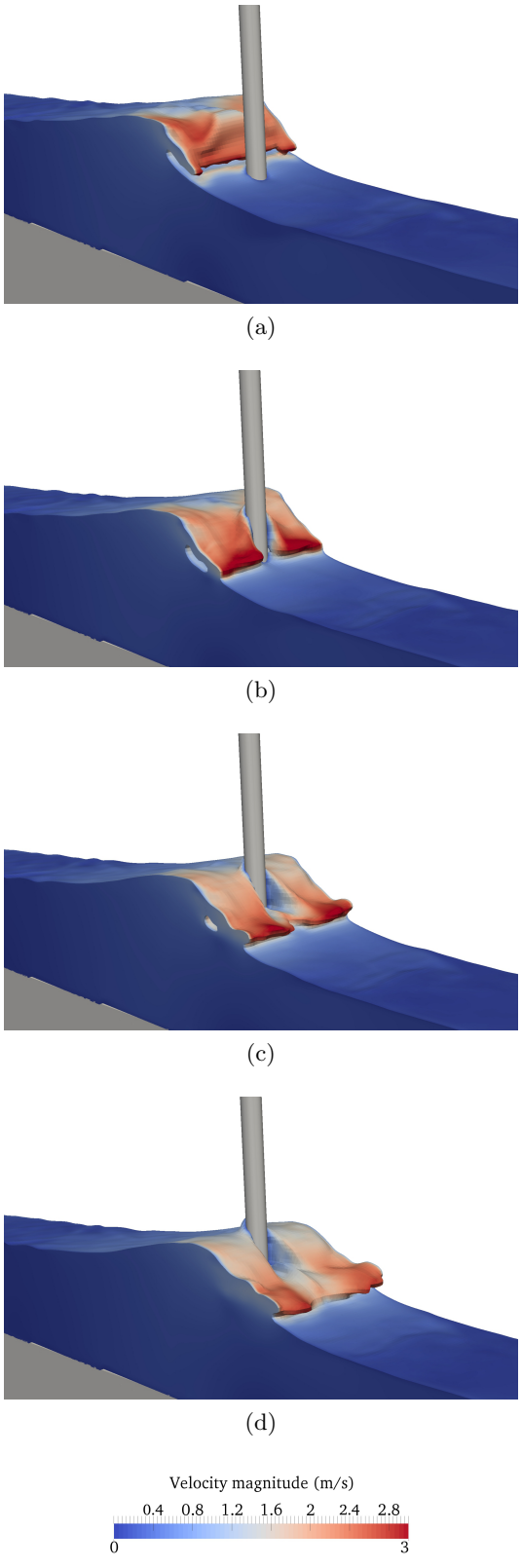

Figure 23: Simulated free surface flow features at t=10.13s, 10.14s, 10.15s and 10.16s for case PL-5 (H_0=0.24m, T=2.22s) and wave impact condition WI-3: wave breaks far before the cylinder.

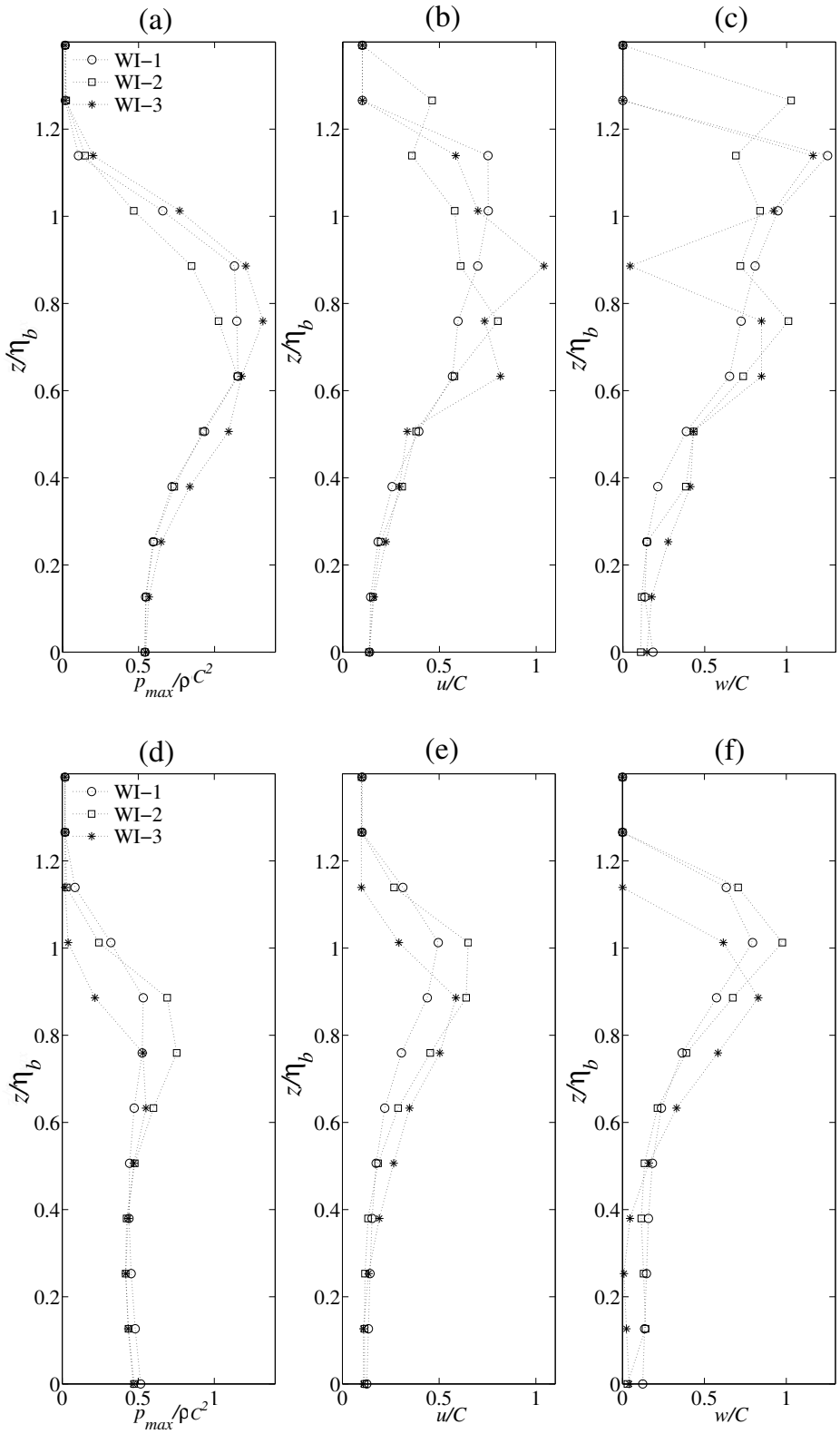

Figure 24: Computed vertical variation of normalized wave impact pressure, horizontal and vertical velocity components versus normalized height for the spilling breaker cases, SP-1 (H_0=0.165m, T=1.90s) and SP-4 (H_0=0.0.183m, T=1.86s) for three impact conditions, WI-1: wave breaks exactly on the cylinder, WI-2: wave breaks ahead of the cylinder and WI-3: wave breaks far before the cylinder.

Like plunging breakers, the largest $p_{max}/\rho C^2$ occurs for the case with low wave steepness (case SP-1) for spilling breakers. In these cases, the maximum wave height at breaking is $1.14H_0$, which is the largest Ω_b of all cases (Fig. 19 (b)). Considering the wave profile at breaking, the wave crest deforms more vertically with a larger wave crest and a shallower wave trough and not much changes in the longitudinal wave crest geometry, corresponding to μ=0.85 and (Fig. 20 (c)) λ=3.50 (Fig. 20 (d)). Further, for plunging breakers, the spatial location at which the maximum u/C appears is just below the level of maximum $p_{max}/\rho C^2$. In contrast, the maximum u/C and w/C velocity components occur above the level of the maximum $p_{max}/\rho C^2$ for spilling breakers. This implies that the plunging breaking wave impact is associated with a higher wave crest with a steep overturning wave crest. On the other hand, for spilling breakers, the breaking wave at the impact has a relatively smaller overturning crest with a less steep wave front. Interestingly, the largest w/C occurs when the wave breaks exactly on the cylinder except for case SP-4. Moreover, the vertical position at which the maximum w/C occurs is always higher than the maximum wave surface elevation at breaking (i.e. $z/\eta_b > 1$) for all impact conditions for both breakers. In particular, the level at which the maximum w/C occurs is always higher than the maximum wave surface elevation at breaking. This is due to a rise in water level ahead of the cylinder causing the wave run-up around the cylinder which is also consistent with the experimental observations by Andersen et al. (2011).

4.2.3 Longitudinal variation of maximum wave impact pressure and velocity components

The computed longitudinal variation of maximum normalized pressure and the resulting normalized horizontal and vertical velocity components versus the normalized distance (x_w/L_b) for cases PL-1 and PL-5 are presented in Fig. 26 for three impact conditions. The probe locations R1 to R8 as shown in Fig. 25 are used to compute the pressure and velocity components. The positive values of x_w/L_b represent the downstream positions behind the cylinder and the negative values denote the upstream positions ahead of the cylinder. After the wave interacts with the cylinder, it loses most of its energy. The percentage of difference between upstream and downstream values for $p_{max}/\rho C^2$, u/C and w/C are listed in Table 3. As mentioned in Section 4.2, the largest pressure $p_{max}/\rho C^2$ occurs for conditions WI-2 and WI-3 for cases PL-1 and PL-5, respectively. It appears that for both cases, $p_{max}/\rho C^2$ increases gradually as the wave approaches the cylinder until x_w/L_b=-0.04 and then it increases suddenly in front of the cylinder for all impact conditions. In fact, the wave height starts to decrease after the breaking point with a forward overturning wave crest (Fig.22 (b) and (c)) in the wave propagation direction. It is also noticed that the horizontal velocity component of the overturning wave crest is large as shown in Fig. 13 (a) and (b). When the overturning wave crest impacts the cylinder, the wave crest separates along the cylinder and it reconnects further downstream (Fig.22 (c) and (d)). As a result, a sudden drop in the pressure and in the velocity components occur in the shadow region right behind the cylinder.

A series of snapshots of numerically modeled free surface flow features during the breaking wave interaction for case PL-5 under the wave condition WI-3 is depicted in Fig. 23. In this case, the wave with a fully developed overturning wave crest hits the cylinder at the forward trough level and the wave front is separated as it interacts with the cylinder (Fig.23 (b) and (c)). It is also noticed that the reconnection of the deformed free surface takes place further downstream (Fig.23 (d)) compared to the flow scenario for case PL-1 and condition WI-2 (Fig.22 (d)). For all impact conditions, $p_{max}/\rho C^2$ at x_w/L_b=0.012 is nearly 28% smaller when compared to $p_{max}/\rho C^2$

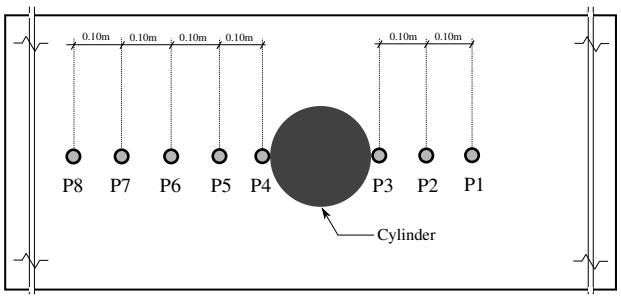

Figure 25: Top view of prob locations in front of the cylinder for analyzing the longitudinal variations.

at x_w/L_b=-0.012. Whereas for case PL-5, except at the position in front of the cylinder, $p_{max}/\rho C^2$ acting on the cylinder is relatively larger when the wave breaks ahead of it and interacts with an overturning wave crest.

Breaker type	Impact conditions	% of difference		
		$p_{max}/\rho C^2$	u/C	w/C
PL-1	WI-1	71	39	63
	WI-2	70	-28	5
	WI-3	76	93	20
PL-5	WI-1	66	86	74
	WI-2	72	88	73
	WI-3	76	90	70
SP-1	WI-1	58	93	78
	WI-2	56	90	79
	WI-3	54	91	79
SP-4	WI-1	32	86	72
	WI-2	52	90	84
	WI-3	40	88	83

Table 3: Computed percentage (%) of difference between the upstream and downstream flow quantities for cases, PL-1 (H_0=0.24m, T=2.22s), PL-5 (H_0=0.219m, T=2.08s), SP-1 (H_0=0.165m, T=1.90s) and SP-4 (H_0=0.0.183m, T=1.86s) for three impact conditions, WI-1: wave breaks exactly on the cylinder, WI-2: wave breaks ahead of the cylinder and WI-3: wave breaks far before the cylinder.

For both cases Fig. 26 (b) and (e), the largest u/C occurs for condition WI-3 at x_w/L_b=-0.10 for case PL-1 and at x_w/L_b=-0.07for case PL-1. Steep velocity gradients are observed between x_w/L_b=-0.07 and 0.012, and u/C increases as the wave propagates further downstream. The horizontal velocity drops suddenly right behind the cylinder (x_w/L_b=0.012), and it increases continuously as the broken wave approaches the shore. During the interaction; the overturning wave crest impacts the cylinder followed by the main wave crest. Meanwhile the wave front is separated by the cylinder causing a noticeable drop in the pressure and velocity downstream. Then, the separated wave front reunites farther downstream creating a water jet behind the cylinder with higher tip velocity as shown in Fig.22 (d) and Fig.23 (d).

As can be seen from Fig. 26 (c) and (f), w/C varies gradually from x_w/L_b=-0.13 to -0.04 and attains its maximum value in front of the cylinder in contrast to the variation of u/C. The lowest w/C occurs for conditions WI-2 and WI-3 for cases PL-1 and PL-5, respectively. However, the largest $p_{max}/\rho C^2$ occurred for these conditions. As mentioned in Section 4.2.2, w/C is always greater than u/C at the instant of impact and it reaches the maximum value for WI-1 for all cases. On the downstream side, both u/C and w/C decrease drastically just behind the cylinder, but they slowly increases as the wave travels further shoreward. On the one hand, the largest $p_{max}/\rho C^2$ and u/C are nearly correlated for all impact conditions, but w/C is the lowest for those largest impact conditions (Fig. 26 (c) and (f)). As can be seen in Table 3, the percentage of difference between upstream (in front of the cylinder) and downstream (behind the cylinder) $p_{max}/\rho C^2$ is larger for plunging breakers. In this case, the wave profile at breaking has a 90% wave crest and a 10% wave trough, and also has very steep wave front and rear face, corresponding to ε=1.05 (Fig.20 (a)), δ=0.29 (Fig.20 (b)) and μ=0.90 (Fig.20 (c)). The analysis of the geometric properties reveal that the plunging breaking waves have larger asymmetric wave crests which exert higher impact pressures on the cylinder.

Fig. 27 shows the computed variation of maximum normalized pressure, horizontal and vertical velocity components along the wave tank ahead of and behind the cylinder for three impact conditions for cases SP-1 and SP-4. As mentioned previously, $p_{max}/\rho C^2$ and w/C increase slowly and reach their maximum values at x_w/L_b=-0.012 (just in front of the cylinder) for all impact conditions on the upstream side. As the wave propagates downstream behind the cylinder, $p_{max}/\rho C^2$ and w/C increase from x_w/L_b=0.012 to 0.04 and decrease from x_w/L_b=-0.04 to 0.07, but u/C increases continuously after x_w/L_b=0.012. Except for condition WI-1 and case SP-1, u/C shows a slowly

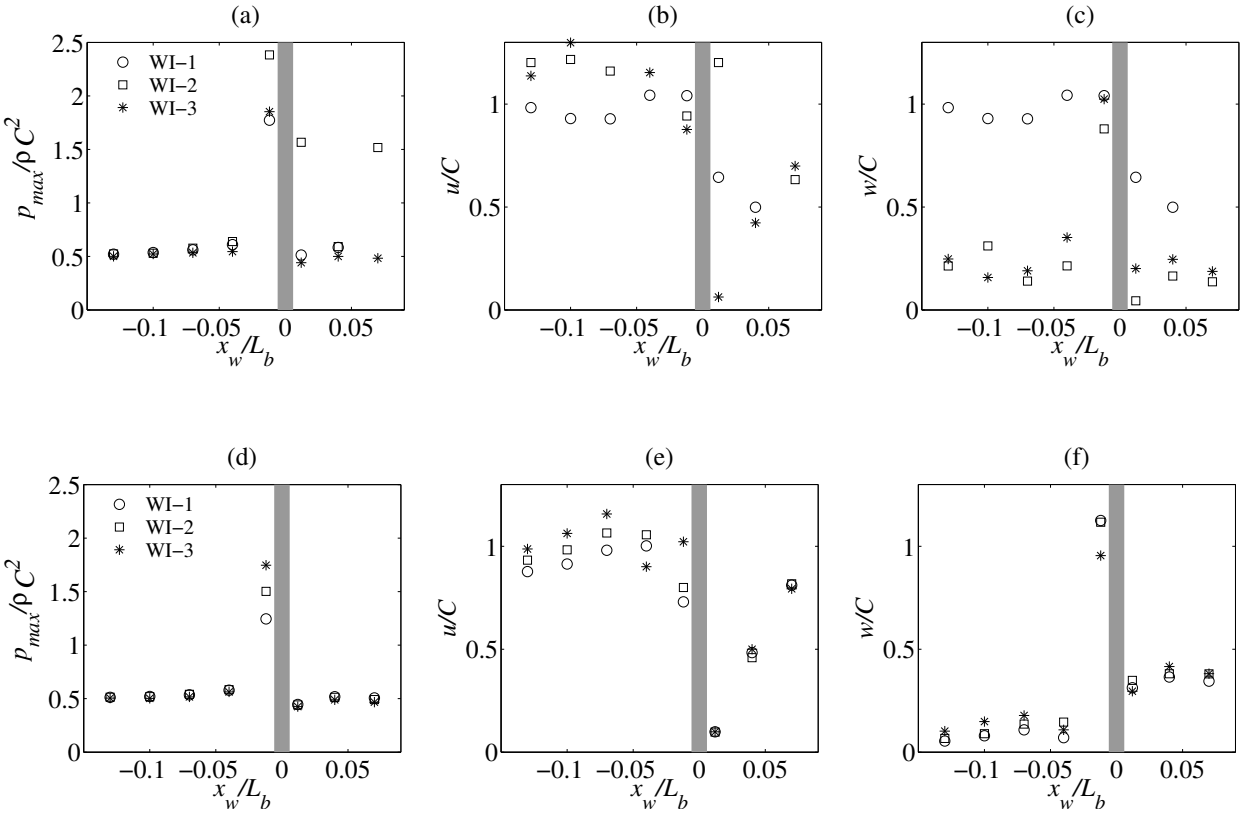

Figure 26: Computed longitudinal variation of normalized wave impact pressure, horizontal and vertical velocity components versus normalized distance (x_w/L_b) for the plunging breaker cases, PL-1 (H_0=0.24m, T=2.22s) and PL-5 (H_0=0.219m, T=2.08s) for three impact conditions, WI-1: wave breaks exactly on the cylinder, WI-2: wave breaks ahead of the cylinder and WI-3: wave breaks far before the cylinder.

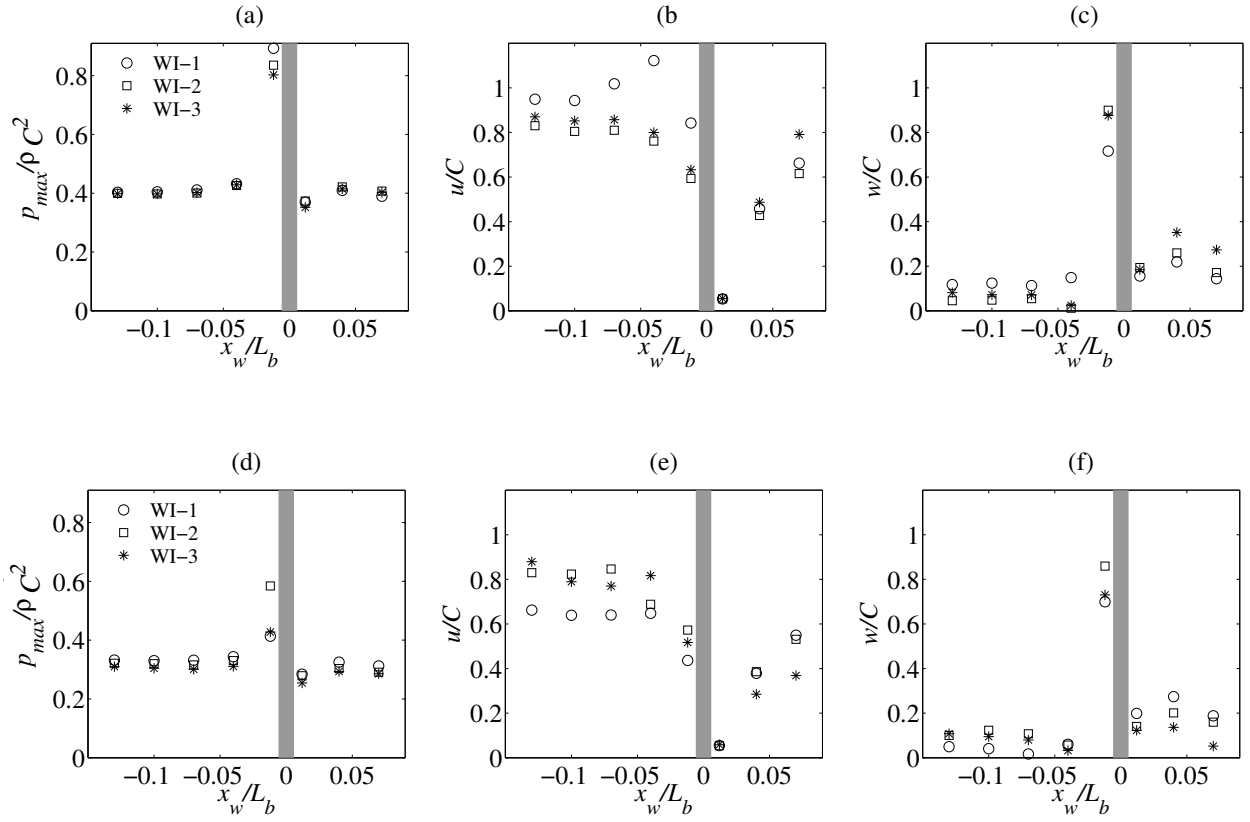

Figure 27: Computed longitudinal variation of normalized wave impact pressure, horizontal and vertical velocity components versus normalized distance (x_w/L_b) for the spilling breaker cases, SP-1 (H_0=0.165m, T=1.90s) and SP-4 (H_0=0.0.183m, T=1.86s) for three impact conditions, WI-1: wave breaks exactly on the cylinder, WI-2: wave breaks ahead of the cylinder and WI-3: wave breaks far before the cylinder.

decreasing trend as the wave approaches the cylinder. Conditions WI-1 and WI-2 yield the largest $p_{max}/\rho C^2$ for cases SP-1 and SP-4, respectively. For the $p_{max}/\rho C^2$ variation, the development of upstream pressure is almost the same for all impact conditions up to x_w/L_b=-0.04.

Particularly, for case PL-1 and condition WI-2, the wave crest at breaking has a high degree of vertical asymmetry (λ) with a relatively steep wave front and a smooth rear part (Fig.20) causing a relatively smaller pressure and velocity gradients downstream. There, the wave crest has a very steep front and rear faces for the case with larger wave steepness (PL-5, Fig. 26 (a)). On the other hand, the difference between upstream and downstream values are nearly the same for $p_{max}/\rho C^2$, u/C and w/C under all impact conditions for spilling breakers. Further, the upstream pressure on the cylinder is around 72% and 48% larger for plunging breakers and spilling breakers, respectively, than for the downstream pressure behind the cylinder. The numerical results clearly show that the impact conditions influence the longitudinal distribution of $p_{max}/\rho C^2$ considerably for plunging breakers, but they marginally affect it for spilling breakers. In contrast to the variation of u/C, $p_{max}/\rho C^2$ and w/C exhibit a similar trend longitudinally and spatially in front of the cylinder (Section 4.1.2). As mentioned in Section 4.2.2, the vertical variations of $p_{max}/\rho C^2$ and u/C follows the same pattern whereas, w/C shows a noticeably different trend. These trends clearly indicate that the wave impact pressure and vertical particle velocity are correlated longitudinally as the wave approaches the cylinder, but at the instant of impact the horizontal velocity follows the pressure pattern vertically.

4.2.4 Total breaking wave forces and maximum wave impact pressure for different impact conditions

Here, the total wave force and maximum impact pressure on the cylinder are computed for spilling and plunging breakers for three different wave impact conditions (Fig. 18). The main focus here is on investigating how the total wave force, the wave impact pressure and the wave impact conditions, as well as the breaker types, are related to each other. Figs. 28 and 29 show the computed normalized total wave force versus time for three impact conditions for plunging and spilling breakers. For plunging breakers, it appears that the largest force occurs under conditions WP-2 and WP-1 for cases PL-1 and PL-5, respectively. Though the lowest force appear for condition WP-3, it has a secondary peak due to the interaction of the curling wave front followed by the main wave crest with the cylinder for PL-1. This feature does not appear for case PL-5. It is evident from the results presented for case PL-1 in Section 4.2.1, that the wave evolves gradually and steadily into a higher and steeper wave crest before it breaks, and a massive amount of wave energy focus near the wave crest. After the breaking point, the wave travels with high velocity by transforming the potential energy into kinematic energy and impinges the cylinder with a moderately developed overturning wave crest. At the same time, for condition WI-3, the wave breaks far before the cylinder and loses more than half of its energy during the breaking and the impingement onto the free surface and the cylinder. This causes a relatively lower pressure gradient along the cylinder and thus a lower total wave force. Although H_0/L_0 is larger for case PL-5, the wave dissipates most of its energy during the breaking imposing lesser wave force on the cylinder than for the case with lower H_0/L_0.
For spilling breakers, the total forces on the cylinder are almost the same for conditions WI-1 and WI-2, and they are slightly larger than for condition WI-3. In contrast to the time profile of the wave impact pressure (Fig. 9 (a)), the total force on the cylinder increases slowly with a longer rise time until the peak, and diminishes gradually with a relatively shorter fall time (Figs. 28 and 29)

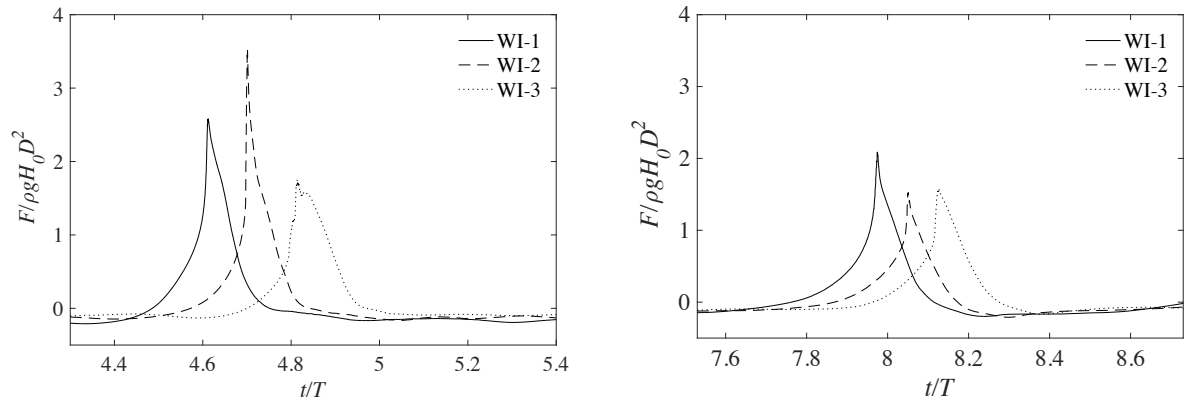

Figure 28: Computed normalized total breaking wave force under three impact conditions for the plunging breaker cases, PL-1 (H_0=0.24m, T=2.22s) and PL-5 (H_0=0.219m, T=2.08s) for three impact conditions, WI-1: wave breaks exactly on the cylinder, WI-2: wave breaks ahead of the cylinder and WI-3: wave breaks far before the cylinder..

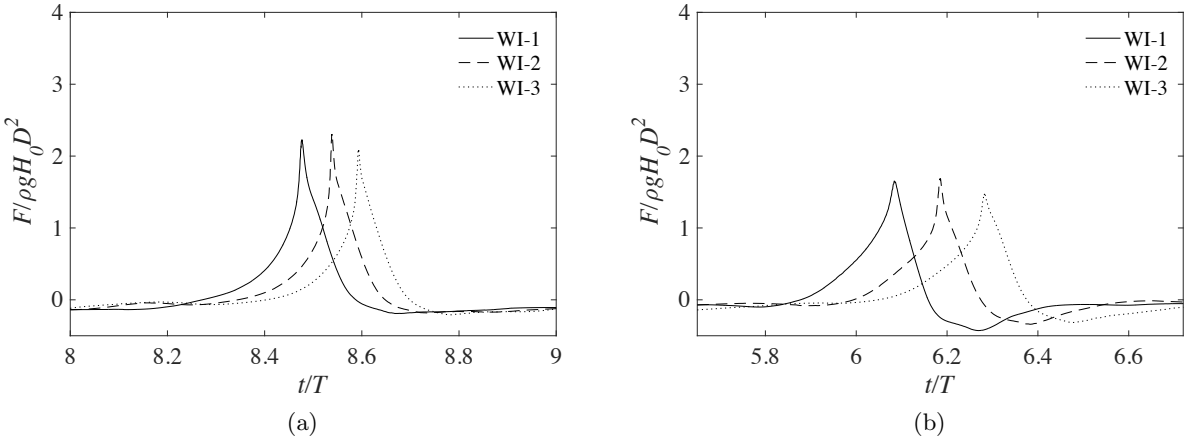

Figure 29: Computed normalized total wave force under three impact conditions for the spilling breaker cases, SP-1 (H_0=0.165m, T=1.90s) and SP-4 (H_0=0.0.183m, T=1.86s) for three impact conditions, WI-1: wave breaks exactly on the cylinder, WI-2: wave breaks ahead of the cylinder and WI-3: wave breaks far before the cylinder.

which nearly resembles the time profile of the vertical velocity (Fig.9 (c)). In general, the total wave force from breaking waves consists of the quasi-static force and the wave impact force of very short duration. Therefore, the peak of the wave impact pressure is significantly sharper than the peak of the total force. Moreover, the wave impact pressure is computed instantaneously at a given point on the cylinder, whereas the total breaking wave force is obtained by integrating the pressure around the cylinder. However, as discussed in Section 4.2.3, the difference in pressure between the upstream

and downstream sides of the cylinder is considerably larger for breaking waves, particularly for the plunging breakers.

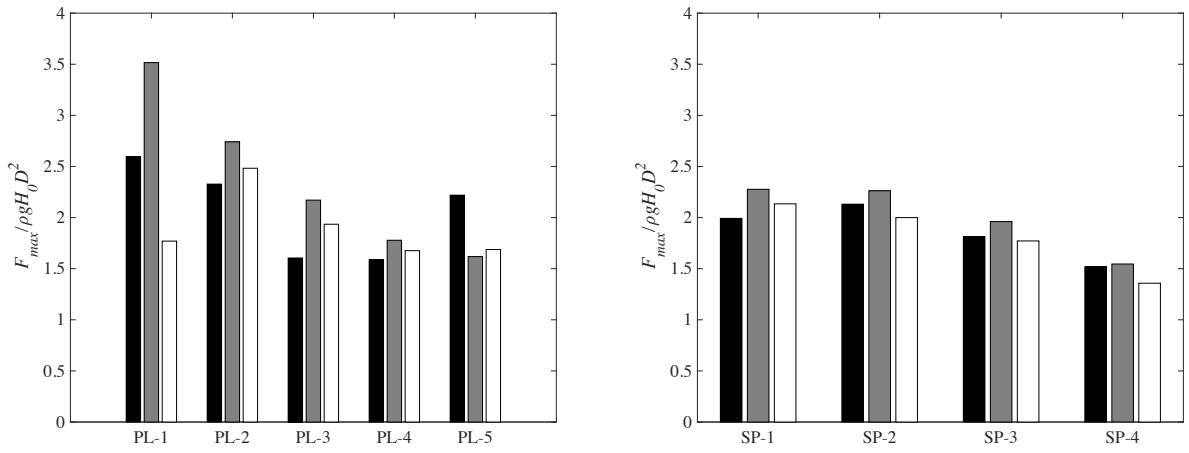

Figure 30: Computed normalized total wave force for (a) plunging breakers and (b) spilling breakers for three impact conditions, WI-1: wave breaks exactly on the cylinder, WI-2: wave breaks ahead of the cylinder and WI-3: wave breaks far before the cylinder. Black columns: WI-1, grey columns: WI-2 and white columns: WI-3.

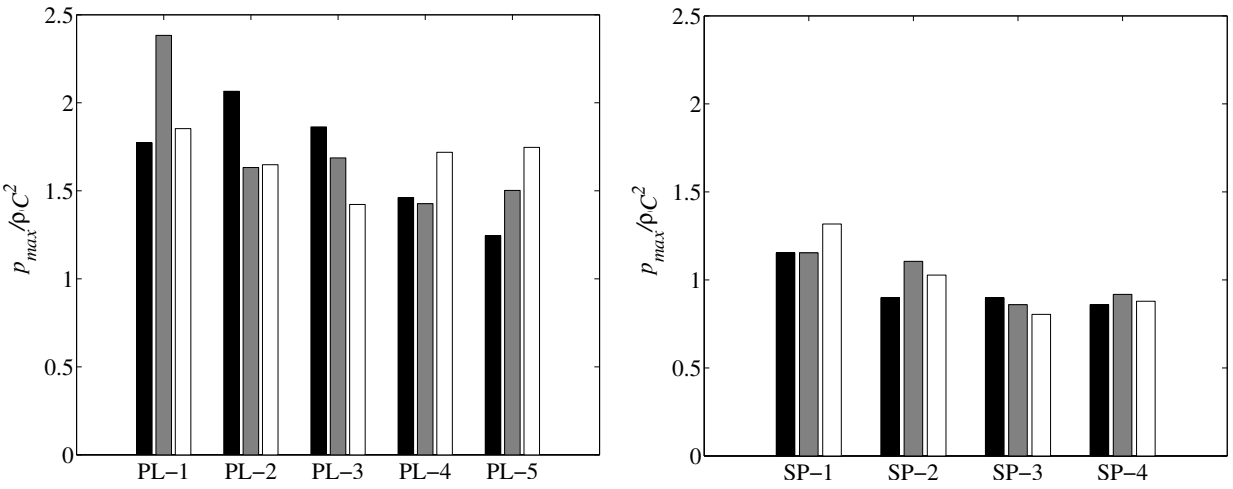

Figure 31: Computed normalized maximum impact pressure for (a) plunging breakers and (b) spilling breakers for three impact conditions, WI-1: wave breaks exactly on the cylinder, WI-2: wave breaks ahead of the cylinder and WI-3: wave breaks far before the cylinder. Black columns: WI-1, grey columns: WI-2 and white columns: WI-3.

Figs. 30 and 31 present the normalized maximum total wave force and the normalized maximum wave impact pressure ($p_{max}/\rho C^2$) on the cylinder for each case under different impact conditions for plunging and spilling breakers. Except for the plunging breakers in case PL-5, the largest wave force occurs when the breaking wave hits the cylinder (WI-2) with a moderately evolved curling wave crest. However, in general, the normalized maximum total wave force (Fig. 30) and the normalized maximum impact pressure (Fig. 31) on the cylinder decrease as the offshore wave steepness (H_0/L_0) increases for both breakers. For the spilling breaker case (SP-1) with the smallest wave steepness, the wave geometry at breaking shows a high degree of horizontal asymmetry with a larger wave crest and a shallower forward trough, corresponding to μ= 0.72 (Fig. 20 (c) and λ=3.55 (Fig. 20 (d)). It should be noted that the largest breaker height index is obtained (Ω_b) for the case with the lowest wave steepness (case SP-1, Table 2) which is Ω_b=1.2 (Fig. 19 (b)). The computed results also suggest that the maximum total force is not directly correlated with the maximum impact pressure on the cylinder. For instance, the cylinder experiences the largest total force when the wave hits it with an overturning wave crest (condition WI-2) for cases PL-2 and PL-3, but the corresponding largest $p_{max}/\rho C^2$ occurs when the wave breaks exactly on the cylinder (conditions WI-1). It is evident that the variation of total breaking wave forces and wave impact pressures under different impact conditions are quite substantial for plunging breakers compared to spilling breakers.

5 Discussion

The breaking characteristics (γ_b and Ω_b), breaking wave celerity (C_b), geometrical properties at breaking (ε, δ, μ and λ), normalized wave impact pressure ($P_{max}/\rho C^2$) and normalized total force ($F_{max}/\rho g H_0 D^2$) for different breakers and impact conditions are presented in Table 4. This provides an overview of various breaking wave properties with respect to the maximum impact pressure, breaking wave kinematics and total forces.

Sim. Cases	L_b/L_0	C_b	γ_b	Ω_b	ε	δ	μ	λ	WIC	$p*$	$F*$
PL-1	0.52	2.26	0.83	1.08	0.68	0.139	0.734	4.89	WI-1	1.80	2.62
									WI-2	1.85	3.51
									WI-3	2.45	1.73
PL-2	0.55	2.24	0.77	1.10	0.69	0.142	0.76	4.87	WI-1	2.12	2.38
									WI-2	1.60	2.72
									WI-3	1.61	2.48
PL-3	0.61	2.31	0.82	1.06	0.81	0.168	0.78	4.82	WI-1	2.10	1.54
									WI-2	1.70	2.15
									WI-3	1.41	1.95
PL-4	0.63	2.27	0.76	1.04	0.89	0.18	0.79	4.82	WI-1	1.48	1.55
									WI-2	1.46	1.61
									WI-3	1.65	1.58
PL-5	0.70	2.31	0.85	1.02	0.98	0.21	0.854	4.67	WI-1	1.20	2.20
									WI-2	1.50	1.56
									WI-3	1.72	1.61

SP-1	0.65	2.19	0.63	1.06	0.81	0.16	0.82	3.72	WI-1	1.15	2.0
									WI-2	1.15	2.26
									WI-3	1.40	2.13
SP-2	0.61	2.18	0.62	1.05	0.68	0.18	0.83	3.61	WI-1	0.80	2.08
									WI-2	1.15	2.19
									WI-3	1.07	2.03
SP-3	0.63	2.19	0.61	1.14	0.53	0.16	0.82	3.41	WI-1	0.90	1.82
									WI-2	0.84	2.04
									WI-3	0.81	1.79
SP-4	0.62	2.18	0.61	1.18	0.61	0.15	0.85	3.56	WI-1	0.77	1.48
									WI-2	0.91	1.51
									WI-3	0.82	1.39

Table 4: List of maximum values for breaking wave characteristics (γ_b and Ω_b), geometric properties (ε, δ, μ and λ), normalized maximum wave impact pressure ($p* = p_{max/\rho C^2}$) and normalized forces ($F* = F/\rho g H_0 D^2$).

Although the wave impact is a highly localized phenomenon, the reason for higher wave loads on the cylinder for waves with low offshore wave steepness (H_0/L_0) is indirectly related to the incident wave conditions. During shoaling, the initial wave characteristics influence the wave transformation process on the slope. As mentioned in Section 4.2.4, the incident wave height is nearly the same for all cases for each breaker group, while the wave period changes. Therefore, the smaller the offshore steepness the larger the wave length and thus, the longer the interaction with the slope during shoaling due to a deeper wave base (i.e. one half of a wave length). As a result, the waves deform more; the wave crest becomes wider and higher and the wave trough becomes deeper with decreasing H_0/L_0, corresponding to Ω_b=1.1(Fig. 19 (b)), μ= 0.72 (Fig. 20 (c)) and λ= 4.90 (Fig. 20 (d)). In fact, the wave length of a wave affects its celerity in shallow waters; the waves with a longer wave length (smaller H_0/L_0) propagate faster than the wave with a shorter wave length (larger H_0/L_0). It should be noted that L_b/L_0 decreases as the wave steepness increases (Table 4) for the plunging breakers. In the present case, the smaller the offshore steepness the larger the wave length and thus, the faster the water mass hits the cylinder.

Cases	Impact condition, WI-1			Impact condition, WI-2			Impact condition, WI-3		
	IR (η_{max})	PL (η_{max})	p_{max} (ρC^2)	IR (η_{max})	PL (η_{max})	p_{max} (ρC^2)	IR (η_{max})	PL (η_{max})	p_{max} (ρC^2)
Chan et al. (1995)	—	0.94	2.0	—	0.81-0.94	6.0-17.0	—	0.54-0.67	5.0-13.0
Hildebrandt (2013)	0.7-1.3	1.0	5.0	0.7-1.2	0.90-1.0	3.0	0.6-1.1	0.8	2.0

Present study (PL-1)	0.3-1.1	0.65	1.8	0.3-0.9	0.65	2.40	0.2-0.7	0.5	1.85

Table 5: Comparison between the numerical results and the experimental results by Chan et al. (1995) and Hildebrandt (2013) for the vertical distribution of wave impact pressure on a vertical cylinder. IR is the impact region; PL is the peak location; p is the peak pressure.

The computed pressure profiles are consistent with these experimental studies; the vertical location of the peak pressure for each case and impact condition is slightly lower than those measured. Table 5 compares the numerical results (case PL-1) with the laboratory measured data by Chan et al. (1995), Hildebrandt (2013), Hildebrandt and Schlurmann (2012) for the vertical distribution of wave impact pressure on a vertical cylinder for three impact conditions.
It should be noted that the model setup, structural configuration, water depth condition and wave type in the present study are significantly different from these laboratory studies. In order to give an overview of the findings of the present study, the numerical results (case PL-1) are compared with these experimental studies. The computed span of the impact region (IR) is almost equivalent to the one measured by Hildebrandt (2013) for all impact conditions. Then the computed largest wave impact pressures and the corresponding peak locations for all three impact conditions are lower than those of Chan et al. (1995) and Hildebrandt (2013). It is possible that both experimental studies are based on breaking focused wave packets which possess a distinct main wave crest when compared to the rest the wave components, whereas the present investigation is based on breaking regular shallow water waves. Moreover, the scaling of the wave parameters at the wave paddle and breaking are not straight forward since the kinematic and dynamic scales of the flow are different in spatial and temporal variations. However, the comparison shows that the main findings of the present study is reasonably consistent with the previous experimental studies.

6 Conclusions

This paper has investigated the breaking wave interaction with a vertical cylinder placed over a submerged structure using the open-source computational fluid dynamic model REEF3D. The model solves the incompressible Reynolds-Averaged Navier-Stokes (RANS) equations together with the level set method for free surface and $k-\omega$ for turbulence. The main focus of the study was to investigate the influence of wave steepnesses and impact conditions on the wave impact pressure and velocity components in the vicinity of a vertical cylinder and the resulting total breaking wave forces. The performance of the numerical model was evaluated by comparing the numerical results with experimental data, and good agreement was obtained for the wave surface elevation at breaking, the total breaking wave forces and the wave characteristics and celerity at breaking. The spatial and temporal evolution of the maximum pressure profile in front of the cylinder and the associated velocity profiles were examined. Three breaking wave impact conditions were considered in this study: (a) when the wave breaks at the cylinder, (b) when the wave breaks before the cylinder

and interacts with a moderately developed overturning wave crest, and (c) when the wave breaks far before the cylinder and interacts with a fully developed overturning wave crest. A total of 9 two-dimensional and 27 three-dimensional simulations were performed with plunging and spilling breakers for nine different offshore wave steepnesses. Under the three impact conditions, the vertical and longitudinal variations of wave impact pressure and velocity components were computed around the cylinder for each breaker type. Moreover, the simulated free surface deformations in the vicinity of the cylinder during the wave impact were presented for selected cases. Based on the detailed numerical investigations, the following findings can be summarized:

- The impact pressure rise time increases with increasing offshore wave steepness. For a given impact condition and offshore steepness, the vertical velocity first reaches its maximum value followed by the horizontal velocity and the pressure.
- The computed temporal and spatial development of the wave impact pressure profiles indicate that the steep pressure gradients tend to occur during the wave impact on the cylinder in a very short distance (order of 0.025m) and time (order of 5 milliseconds). Meanwhile, unlike the temporal variation of the vertical velocity, its spatial variation is correlated with the pressure. However, the horizontal velocity gradients are relatively smaller than the pressure gradients.
- When the broken wave advances towards the cylinder, the wave motion is retarded in front of the cylinder. Thus, the time profile of the pressure becomes higher and wider, whereas the horizontal velocity profile becomes narrower and sharper. The vertical distribution of the maximum wave impact pressure on the cylinder and the corresponding velocity components vary significantly along the depth above the still water level for the different impact conditions.
- For all impact conditions, the longitudinal variation of the wave impact pressure and the vertical velocity component are correlated when the breaking wave approaches the cylinder, but at the instant of impact the vertical profile of the horizontal velocity component follows the pressure pattern.
- It is found that the maximum values of the wave impact pressure and the associated vertical velocity component tend to occur at the instant of wave impact, whereas the maximum horizontal velocity is most likely to occur farther ahead of the cylinder. Although the upstream and downstream pressure gradients are larger for plunging breakers, the velocity gradients are slightly lower than for spilling breakers.
- The largest breaking wave force occurs for the impact condition when the wave breaks ahead of the cylinder and impacts with a moderate overturning wave crest for different offshore wave steepnesses. However, the wave impact condition at which the maximum impact pressure occurs is different for each case. These variations suggest that the wave impact conditions have a significant influence on the total breaking wave force and the maximum wave impact pressure for plunging breakers compared to spilling breakers.

Acknowledgment

The research work has been funded by the Research Council of Norway through the project "Hydrodynamic Loads on Offshore Wind Turbine Substructures due to Nonlinear Irregular Breaking, High Steep and Extreme Waves" (project number: 246810). The authors would like to thank Assoc. Prof.

Øivind A. Arntsen and Mr. Xavier Ros Collados for sharing the experimental data.The authors gratefully acknowledge the computing time granted by NOTUR (project number: NN2620K).

References

Alagan Chella, M., Bihs, H. and Myrhaug, D. (2015b). Characteristics and profile asymmetry properties of waves breaking over an impermeable submerged reef. *Coast. Eng.*, **100**, 26–36.

Alagan Chella, M., Bihs, H., Myrhaug, D. and Muskulus, M. (2015a). Breaking characteristics and geometric properties of spilling breakers over slopes. *Coast. Eng.*, **95**, 4–19.

Alagan Chella, M., Bihs, H., Myrhaug, D. and Muskulus, M. (2016). Hydrodynamic characteristics and geometric properties of plunging and spilling breakers over impermeable slopes. *Ocean Modelling*, **103**, 53–72.

Alagan Chella, M., Bihs, H., Myrhaug, D. and Muskulus, M. (2017). Breaking solitary waves and breaking wave forces on a vertically mounted slender cylinder over an impermeable sloping seabed. *Journal of Ocean Engineering and Marine Energy*, **3**, 1–19.

Alagan Chella, M., Tørum, A. and Myrhaug, D. (2012). An overview of wave impact forces on offshore wind turbine substructures. *Energy Procedia*, **20**, 217–226.

Andersen, T., Frigaard, P., Damsgaard, M. and De Vos, L. (2011). Wave run-up on slender piles in design conditions - Model tests and design rules for offshore wind. *Coast. Eng.*, **58**, 281–289.

Arntsen, Ø.A., Ros, X. and Tørum, A. (2011). Impact forces on a vertical pile from plunging breaking waves. In: *Proceedings of the 24-th Conference on Coastal Structures*.

Ashby, S.F. and Falgout, R.D. (1996). A parallel multigrid preconditioned conjugate gradient algorithm for groundwater flow simulations. *Nuclear Science and Engineering*, **124**(1), 145–159.

Basco, D.R. (1985). A qualitative description of wave breaking. *J. Waterw. Port Coast. Ocean Eng.*, **3**(2), 171–188.

Berthelsen, P.A. and Faltinsen, O.M. (2008). A local directional ghost cell approach for incompressible viscous flow problems with irregular boundaries. *J. Comput. Phys.*, **227**, 4354–4397.

Bihs, H. and Kamath, A. (2017). A combined level set/ghost cell immersed boundary representation for floating body simulations. *International Journal for Numerical Methods in Fluids*, **83**, 905–916.

Bihs, H., Kamath, A., Alagan Chella, M., Aggarwal, A. and Arntsen, Ø.A. (2016*a*). A new level set numerical wave tank with improved density interpolation for complex wave hydrodynamics. *Computers and Fluids*, **140**, 191–208.

Bihs, H., Kamath, A., Alagan Chella, M. and Arntsen, Ø.A. (2016*b*). Breaking wave interaction with tandem cylinders under different impact scenarios. *J. Waterw. Port Coast. Ocean Eng.* DOI: 10.1061/(ASCE)WW.1943-5460.0000343.

Bredmose, H., Bullock, G. and Hogg, A. (2015). Violent breaking wave impacts. Part 3. effects of scale and aeration. *Journal of Fluid Mechanics*, **765**, 82–113.

Bredmose, H. and Jacobsen, N.G. (2010). Breaking wave impacts on offshore wind turbine foundations: Focused wave groups and CFD. In: *Proceedings of the 29-th International Conference on Ocean, Offshore and Arctic Engineering*, 397–404.

Bredmose, H. and Jacobsen, N.G. (2011). Vertical wave impacts on offshore wind turbine inspection platforms. In: *Proceddings of the 30-th International Conference on Ocean, Offshore and Arctic Engineering*, 645–654.

Camp, T., Morris, M., Van Rooij, R., Van Der Tempel, J., Zaaijer, M., Henderson, A. and et al. (2003). Design methods for offshore wind turbines at exposed sites. Technical report, Garrad Hassan and Partners Ltd., Bristol, UK.

Chakrabarti, S.K., Kriebel, D. and Berek, E. (1997). Forces on a single pile caisson in breaking waves and current. *Appl Ocean Res*, **19**, 113–140.

Chan, E.S., Cheong, H. and Tan, B. (1995). Laboratory study of plunging wave impacts on vertical cylinders. *Coast. Eng.*, **25**, 87–107.

Choi, S., Lee, K. and Gudmestad, O. (2015). The effect of dynamic amplification due to a structures vibration on breaking wave impact. *Ocean Eng.*, **96**, 8–20.

Chorin, A. (1968). Numerical solution of the Navier-Stokes equations. *Math. Comput.*, **22**, 745–762.

Christensen, E.D., Bredmose, H. and Hansen, E.A. (2005). Extreme wave forces and wave run-up on offshore wind turbine foundations. In: *Proceedings of Copenhagen Offshore Wind*, 1–10.

Cokelet, E. (1977). Breaking waves. *Nature*, **267**, 769–774.

Falgout, R.D., Jones, J.E. and Yang, U.M. (2006). *The Design and Implementation of hypre, a Library of Parallel High Performance Preconditioners*, 267–294. Springer Berlin Heidelberg.

Fenton, J.D. (1999). *The cnoidal theory of water waves*, chapter 2, 55–100. Developments in Offshore Engineering, Gulf, Houston. Herbich. J. B. (Ed.) edition.

Ghadirian, A., Bredmose, H. and Dixen, M. (2016). Breaking phase focused wave group loads on offshore wind turbine monopiles. In: *Journal of Physics: Conference Series*, volume 753.

Goda, Y. (2010). Reanalysis of regular and random breaking wave statistics. *Coast. Eng. Journal*, **52**(01), 71–106. ISSN 0578-5634.

Goda, Y., Haranaka, S. and Kitahata, M. (1966). Study of impulsive breaking wave forces on piles. Technical report, Port and Harbor Research Institute, Ministry of Transport.

Griebel, M., Dornseifer, T. and Neunhoeffer, T. (1998). *Numerical Simulation in Fluid Dynamics, a Practical Introduction*. SIAM.

Hildebrandt, A. (2013). *Hydrodynamics of breaking waves on offshore wind turbine structures*. Ph.D. thesis, Leibniz Universität Hannover.

Hildebrandt, A. and Schlurmann, T. (2012). Breaking wave kinematics, local pressures, and forces on a tripod structure. In: *Proceedings of the 33rd Conference on Coastal Engineering*, 1–14.

Irschik, K., Sparboom, U. and Oumeraci, H. (2002). Breaking wave characteristics for the loading of a slender pile. In: *Proceedings of the 28-th Conference on Coastal Engineering*, 1341–1352.

Jacobsen, N.G., Fuhrman, D.R. and Fredsøe, J. (2012). A wave generation toolbox for the open-source CFD library : OpenFoam. *Int. J. Numer. Methods Fluids*, **70**, 1073–1088.

Jiang, G.S. and Shu, C.W. (1996). Efficient implementation of weighted ENO schemes. *J. Comput. Phys.*, **126**, 202–228.

Kamath, A., Alagan Chella, M., Bihs, H. and Arntsen, Ø.A. (2016). Breaking wave interaction with a vertical cylinder and the effect of breaker location. *Ocean Eng.*, **128**, 105–115.

Kjeldsen, S.P. and Myrhaug, D. (1978). Kinematics and dynamics of breaking waves. Technical report, River and Harbour Laboratory (NHL), The Norwegian Institute of Technology.

Larsen, J. and Dancy, H. (1983). Open boundaries in short wave simulations - a new approach. *Coast. Eng.*, **7**, 285–297.

Lin, P. (2008). *Numerical modeling of water waves.* CRC Press.

Miller, R.L. (1987). Role of vortices in surf zone prediction: sedimentation and wave forces. *The Society of Economic Paleontologists and Mineralogists, Special Publications*, (24), 92–114.

Miquel, A.M., Kamath, A., Alagan Chella, M., Archetti, R. and Bihs, H. (2018). Analysis of different methods for wave generation and absorption in a CFD-based numerical wave tank. *Journal of Marine Science and Engineering*, **6**, 1–21.

Ochi, M.K. and Tsai, C.H. (1984). Prediction of impact pressure induced by breaking waves on vertical cylinders in random seas. *Applied Ocean Research*, **6**(3), 157 – 165.

Peregrine, D.H., Cokelet, E.D. and Mclver, P. (1980). The fluid mechnics of waves approaching breaking. In: *Proceedings of the 17-th Conference on Coastal Engineering*, 512–528.

Sawaragi, T. and Nochino, M. (1984). Impact forces of nearly breaking waves on a vertical circular cylinder. *Coastal Engineering Journal*, **27**, 249–263.

Schäffer, H.A. and Klopman, G. (2000). Review of multidirectional active wave absorption methods. *J. Waterw. Port Coast. Ocean Eng.*, **126**, 88–97.

Shu, C.W. and Osher, S. (1988). Efficient implementation of essentially non-oscillatory shock capturing schemes. *J. Comput. Phys.*, **77**, 439–471.

Weggel, J.R. (1972). Maximum breaker height for design. In: *Proceedings of the 13-th Conference on Coastal Engineering*, 419–432.

Wienke, J. and Oumeraci, H. (2005). Breaking wave impact force on a vertical and inclined slender pile-theoretical and large-scale model investigations. *Coast. Eng.*, **52**, 435–416.

Wilcox, D.C. (1994). *Turbulence Modeling for CFD.* DCW Industries Inc., La Canada, California.

Yao, Y., Huang, Z., Monismith, S.G. and Lo, E.Y. (2013). Characteristics of monochromatic waves breaking over fringing reefs. *Journal Coastal Research*, **29**(1), 94–104.

Zhou, D., Chan, E. and Melville, W. (1991). Wave impact pressures on vertical cylinders. *Applied Ocean Research*, **13**, 220–234.